AN ABSTRACT OF THE DISSERTATION OF

Rebecca Cullion for the degree of Doctor of Philosophy in Mechanical Engineering presented on December 05, 2005.

Title: Void Fraction Variations in a Fractal-Like Branching Channel Network

Redacted for privacy

Abstract approved:

Deborah Pence

Two-phase flow in a fractal-like branching microchannel heat sink may have enhanced heat transfer capabilities over single phase flow in the same branching channel network. In order to exploit this potential, a complete understanding of flow boiling in this geometry is required. The fractal-like geometry is similar to that of the human circulatory system; a larger diameter channel, or artery, branches into two channels, or arteries, of smaller diameter.

An experimental study of flow boiling in a fractal-like branching channel heat sink was performed. The fractal-like network, fabricated for use in this study, utilized a circular configuration, in which fluid entered the center of the device and flowed radially outward. The resultant, bifurcating pattern is perfectly symmetrical, and has four different branching levels. The channels of the branches range in hydraulic diameter from 218 micron at the inlet to 120 micron at the periphery of the heat sink. High-speed, high-resolution imaging was used to visualize flow regimes and quantify void fraction variations in the channels. Regional and local changes in void fraction were analyzed for the effects of this novel geometry on flow boiling characteristics. Of particular interest was the interaction between different branching levels and the impact of bifurcations on vapor flow.

Global measurements of pressure, temperature, flow rate, and power input were also made. Operating conditions included an inlet temperature of 88°C, inlet mass flow rates between 45 and 65 g/min, and two power levels of 61 W and 66 W.

Flow regimes observed during qualitative analysis of a base case, defined as $q = 66$ W, $\dot{m} = 45$ g/min, and $T_i = 88$°C, included single phase, bubbly, and slug flow. Quantitative analysis of the base case indicate that the levels of the fractal-like device interact; vapor in a downstream channel affects the flow behavior in an associated upstream channel. In addition, bifurcations associated with the fractal-like geometry affects flow characteristics. Bifurcations split downstream vapor flow and redirected vapor flowing upstream. Comparison of base case results with two other cases indicate increased flow rate, and decreased power, independently t produced void fraction variations that followed the same trends as those found in the base case but with different magnitudes and frequencies.

Void Fraction Variations in a Fractal-Like Branching Channel Network

by

Rebecca Cullion

A DISSERTATION

submitted to

Oregon State University

in partial fulfillment of
the requirements for the
degree of

Doctor of Philosophy

Presented December 05, 2005
Commencement June 2006

Doctor of Philosophy dissertation of Rebecca Cullion presented on December 05, 2005

APPROVED:

Redacted for privacy

Major Professor, representing Mechanical Engineering

Redacted for privacy

Head of the Department of Mechanical Engineering

Redacted for privacy

Dean of the Graduate School

I understand that my dissertation will become part of the permanent collection of Oregon State University libraries. My signature below authorizes release of my disseration to any reader upon request.

Redacted for privacy

Rebecca Cullion, Author

ACKNOWLEDGMENTS

I would like to take this opportunity to acknowledge the individuals who made contributions to this work. First, I would like to thank Dr. Deborah Pence for her role as my advisor. Thank you for teaching my undergraduate Thermodynamics class in such a manner that I was inspired to become a professor.

Thank you to Dr. Charles Brunner, Dr. Murty Kanury, Dr. James Liburdy, and Dr. Vinod Narayanan for serving on my committee. Special thanks to Dr. Liburdy and Dr. Narayanan for the use of equipment from their research labs.

Two students contributed a great deal to this project, Greg Mouchka and Jaime Junell. My thanks to both of them for all of their help and the laughs.

I cannot finish without acknowledging truffles, coffee cards, gelato certificates, and twenty dollar bills. Thank you so very much Mom, Dad, Chris, Nan, Cheryl, and Jim. Your thoughtfulness brightened every day. Finally, I would like to thank Kyle for making everything better always.

TABLE OF CONTENTS

TABLE OF CONTENTS (Continued)

LIST OF FIGURES

Figure | Page

LIST OF TABLES

NOMENCLATURE

C_p: specific heat (kJ/kg K)

h_g: vapor enthalpy (kJ/kg)

h_f: fluid enthalpy (kJ/kg)

I: current (A)

$\dot{m}$: mass flux (g/min)

m_l: liquid mass (kg)

m_v: vapor mass (kg)

n: number of branches resulting from a bifurcation

NWP_{data}: number of white pixels in data image

NWP_{base}: number of white pixels in base image

$\dot{Q}$: heat flux (W/cm^2)

R: resistance (Ω)

T_{sat}: saturation temperature (°C)

T_i: inlet temperature (°C)

V_f: volume of liquid (m^3)

V_g: volume of vapor (m^3)

V_I: voltage associated with current measurement (V)

V_v: voltage associated with voltage measurement (V)

W : channel width (μm)

x_e: exit quality

α: apparent void fraction

α_{vol}: apparent void fraction

Void Fraction Variations in a Fractal-Like Branching Channel Network

1. BACKGROUND

In 2005, Motorola unveiled the Razr. This cell phone is smaller than a deck of cards, weighs 95 grams, and has every possible feature, and is a prime example of the current trend towards smaller, more powerful electronics. Powerful electronic devices run hot, making effective cooling crucial. As the size of these devices decrease, the heatsinks used to cool them must also shrink. Heatsinks where heat transfer is the result of fluid flow through microscale channels are one solution currently being explored. The small diameters of the channels allow a large channel density to be achieved and yield larger heat transfer coefficients thereby, maximizing heat transfer while minimizing volume. A clear understanding of flow characteristics in these devices is necessary to exploit their potential.

For a given geometry, the only way to improve the heat transfer of single-phase flow is to increase the flow rate. Higher flow rates demand greater pumping power and the benefit-to-cost ratio, the energy transfer rate divided by the flow power, is decreased. Two-phase flow combines the sensible heating of single-phase flow with latent heating. The combination of these two thermodynamic mechanisms allows a given heat transfer rate to be achieved at a much lower flow rate than would be required if the flow was single phase. Extensive studies of two-phase, macroscale flow have been performed and the findings used to maximize the benefits while limitations such as increased pressure drops, critical heat flux conditions, or flow instabilities are avoided.

Decreasing channel diameter while holding all other conditions fixed, increases flow velocity and decreases the ratio of flow volume to channel surface area. Given a constant Nusselt number, the decrease in diameter associated with moving from a macroscale channel to a microchannel, improves the heat transfer coefficient. Microscale channels also allow a higher channel density than realizable in a macroscale heatsink, increasing the convective surface area per unit volume. Despite these benefits, eventually increasing single-phase microscale heat transfer requires an increase in flow rate. As with macroscale flow, flow boiling offers an alternative. Two-phase flow in microchannels can achieve the same heat transfer rate as single-phase flow at much lower flow rates. In addition, greater temperature uniformity is expected due to the latent heating. Unfortunately, several of the limitations of macroscale two-phase flow have been observed in these microscale configurations as well. Oscillations between single and two-phase flow have been documented, as have oscillations between different flow regimes [1,2,3,4]. Finally, channels that share an inlet plenum often experience flow reversal [1,4].

A perfectly symmetrical, fractal-like branching microchannel geometry has been suggested as an alternative to the naturally asymmetry of a plenum in a parallel channel heatsink [13]. Self-similarity is apparent in the suggested geometry, shown in Fig. 1.1. The term fractal-like is used, because unlike true fractals, the repeated pattern does not continue on to infinity. A key characteristic of this particular design, and inherent to many fractals, is branching. Branching from one large diameter channel into two smaller channels results in an increased flow area. An additional benefit associated with the decreased diameter at each branching level is improved temperature uniformity. The primary drawback of the fractal-like concept is an inability to achieve the same channel density as a parallel channel configuration. Two-phase flow in this geometry has not yet been studied and will be the focus of this work.

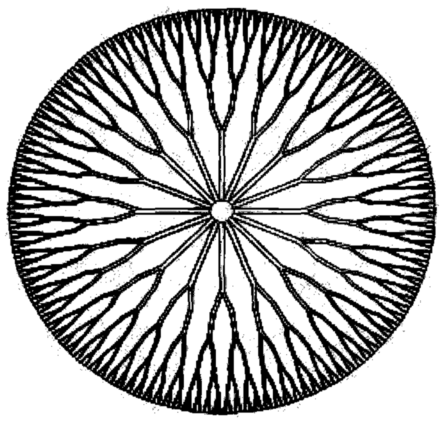

FIGURE 1.1. Fractal-like branching channel network.

There are a few terms specific to this design that should be defined. As can be seen in Fig. 1.1, sixteen channels originate from the inlet plenum. Channel depth in the heat sink studied in this analysis remains constant. Following one of these sixteen channels from the inlet plenum outward, we see that the channel splits into two channels of smaller width and length. The split is referred to as a bifurcation. There are five levels associated with this design as shown in Fig. 1.2. The distance from the first bifurcation to the second is a branching level, there are four such levels. The k = 0 level originates from the inlet plenum rather than from another branch; therefore it is not considered a branching level. The design is split into sixteen even sections, a section contains one k = 0 level channel and is referred to as a tree. Figure 1.2 is an example of a tree.

The objective of this work is to study flow boiling in this fractal-like geometry using high-speed, high-resolution imaging. Flow regimes will be documented and data evaluated for both regional and local void fraction variations. In addition, the effects of this novel geometry will be explored. The impact of bifurcations

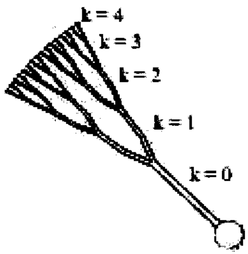

FIGURE 1.2. Tree of a fractal-like branching channel network.

on void fraction, if any, will be studied. The results will be also be examined for interactions between the different branching levels of the geometry. These results will be used to validate a one-dimensional algorithm to be used for optimizing flow geometries for specific operating conditions.

Electronic devices are growing smaller and more powerful. Current cooling capabilities are no longer effective, and increased heat transfer capabilities with minimal size has become crucial. Two-phase flow in microscale heatsinks has shown tremendous potential for fulfilling this need. Use of fractal-like heat sinks offer the potential for significant benefit-to-cost ratios. Other potential applications of the these fractal-like networks include use as desorbers or heat exchangers. A complete understanding of flow boiling in microscale channels must be developed in order to maximize this potential. The focus of this study is to develop an understanding of two-phase flow in a fractal-like branching microchannel geometry.

2. LITERATURE REVIEW AND OBJECTIVES

2.1. Literature Review

2.1.1. Microscale Single Phase Flow

More than twenty years ago Tuckerman and Pease [6] demonstrated the enhanced heat transfer capabilities of a microchannel heatsink. A potential application of this technology is cooling compact, powerful electronic devices. The electrical properties governing the performance of these systems are temperature sensitive, making uniform cooling a necessity. Typical microchannel heatsinks are composed of constant cross-section channels that are subjected to significant axial heating. Bau [7] demonstrated that tapering the cross-sectional area of a microchannel improves temperature uniformity. Unfortunately a trade-off exists, tapering the channels improves surface temperature uniformity but the diminishing cross-sectional area increases the required pumping power.

Mammalian circulatory systems efficiently pump blood throughout the entire body. West et al. [8] proposed that these systems are fractal-like branching networks and developed scaling laws to describe the length and diameter ratios between branching levels. A parallel between metabolic and thermal transport processes was drawn by Pence [9]. By applying the scaling laws of West et al. [8] to a microchannel heatsink design, a fractal-like, branching channel heatsink was generated. The one-dimensional model developed by Pence [10] was used to compare a parallel, straight channel flow network and a fractal-like, branching channel flow network with the same flow power, convective surface area, heat flux, overall channel length, and exit channel width and depth. The fractal-like device experienced pressure drops 35% smaller than the straight channel array. At a bifurcation in the fractal-like design, a single channel branches into two of lesser width. Despite the decrease in hydraulic diameter, the overall flow area is increased, explaining the improved pressure drop performance. Alharbi et al. [11] validated the one-dimensional model results [10] with experimental data and a three-dimensional computational fluid dynamics study.

The fractal-like design used in this study is based on fixed length and width ratios, Eq. 2.1 and Eq. 2.2, where the number of daughter channels that result from a mother channel dictates the value of n. As discussed in Chapter 1, the subscript k refers to a lower order branching level while subscript k+1 represents the higher order branching level at a given bifurcation. The use of a fixed width ratio differs from the original proposal [8] which called for fixed length and diameter ratios. Limitations in manufacturing processes require the fractal-like channels be of uniform depth. This constraint results in lower branching level channels of infinite width when a fixed hydraulic diameter ratio is employed. A fixed width ratio was substituted for the diameter ratio. An optimization method similar to that used by Bejan [12] was used to define that ratio [13].

$$\frac{\mathrm{L_{k+1}}}{\mathrm{L_k}} = \mathrm{n}^{-\frac{1}{2}} \tag{2.1}$$

$$\frac{\mathrm{W_{k+1}}}{\mathrm{W_k}} = \mathrm{n}^{-\frac{1}{2}} \tag{2.2}$$

$$\mathrm{n} = 2 \tag{2.3}$$

Single phase flow studies have shown that the limitations associated with a parallel channel configuration, specifically large pressure drop and surface temperature non-uniformity, do not occur or occur to a lesser degree in the fractal-like device. These studies need to be extended to two-phase flow.

2.1.2. Macroscale Two-Phase Flow

In terms of heat transfer, two-phase flow is an attractive alternative to single-phase flow. Unfortunately, it is not without limitations, including the possibility of unstable flow. Instabilities in heat exchanger flow can result in pressure fluctuations and dry-out, greatly affecting overall performance.

Small fluctuations in the flow can occur during phase change. The flow can either return to its normal operating conditions or these fluctuations can result in instabilities (Boure et al. [14]). Saha and Zuber [15] evaluated the effects of mass flow rate, heat flux, and system pressure on the onset of significant void (OSV), an indicator of onset of flow instability (OFI). Onset of significant void was dictated by thermal conditions at low mass flow rate conditions. Kennedy et al. [16] studied two-phase flow of deionized water in a single, macroscale channel. Effects of varying mass flow rate and heat flux on the OSV were evaluated, and an equation was developed to predict the heat flux at which OSV, and therefore OFI, would occur. In addition, flow reversal was observed in two-phase water flow in a rectangular channel of hydraulic diameter equal to 0.75 mm by Warrier and Dhir [17]. These studies and others like them provided the understanding of two-phase flow necessary to maximize heat transfer in macroscale heat exchangers while avoiding potential issues such as flow instabilities.

2.1.3. Microscale Two-Phase Flow

Two potential issues associated with two-phase flow in microchannels, large pressure drops associated with the phase change and instabilities similar to those seen on the macroscale, have been observed in preliminary studies. Nucleate boiling of a subcooled refrigerant in a parallel channel device resulted in a pressure change one thousand times larger than that measured for single phase flow in the system [18]. Koo et al. [19] saw the pressure drop in a single microchannel increase by 360% after the onset of boiling. Pressure increases of these magnitudes would negate the benefits associated with two-phase flow.

As was mentioned earlier, onset of significant void is indicative of an instability. Therefore, quantifying void fraction variations in microchannels is of importance. Void fraction in a horizontal pipe is defined by Wilkes [20] as the portion of the total pipe volume occupied by the gas phase. Tong and Tang [21] assume one-dimensional flow and report void fraction averaged over the cross-sectional channel area as a ratio of the gas area to cross-sectional flow area. The first definition approaches void fraction from a volumetric standpoint, while the other uses a ratio of areas. Expressing void fraction in terms of areas is of interest because although several void fraction measurement methods exist, the most common, and the one employed by this study, relies on two-dimensional images.

The techniques employed when using images to quantify void fraction were reviewed to determine the requirements for measuring a three-dimensional quantity with a two-dimensional method. Triplett et al. [22] performed a two-phase flow void fraction study in circular and semi-triangular microchannels. The working fluid was an air and water mixture, and the flow was assumed to be one-dimensional and steady state. To quantify the void fraction, each bubble was assigned a geometric shape that best represented the actual shape. The volume of the bubble was calculated using the assigned shape and visible dimensions. These measurements compared well to homogeneous flow model predictions. Chung et al. [23] imaged two-phase flow of nitrogen and water in mini and microchannels. In the minichannel, the two-dimensional shape of the bubble was related to a symmetrical volume and the fraction of gas estimated. In the microchannel, it was assumed there was no bubbly flow and all images for a given experiment were assigned a void fraction. All liquid flow was considered to have a void fraction of zero, while annular flow with a very thin liquid film was considered to have a void fraction of unity. Void fraction of annular flow with a thick liquid film is determined by assuming the gas is a cylinder, and taking the ratio of the gas cylinder radius squared to the channel radius squared. The void fractions for each image were summed and divided by the total number of pictures to determine a time averaged void fraction.

By quantifying void fraction in a manner similar to the methods just discussed, the results can be evaluated for onset of significant void and, therefore, onset of flow instability. Of the microscale liquid/vapor flow imaging studies reviewed, all reported instabilities. Steinke and Kandlikar [1] investigated two-phase flow of deionized water in a heatsink with six parallel microchannels. The channels were rectangular in cross-section with hydraulic diameters of 207 μm. The flow rate was held constant while the heat flux was increased incrementally and images recorded at 500 frames per second (fps). The flow oscillated between bubbly and annular and counter-flow due to pressure fluctuations, and communication between the parallel channels were observed. The interaction of surface tension, inertia, and evaporation momentum forces resulted in this flow reversal (Kandlikar [24]). Jiang and Wong [2] performed a two-phase flow visualization study of deionized water in two different microchannel heatsinks. Both devices had multiple parallel channels, with hydraulic diameters ranging from 26 to 35 μm. Varying the flow rates and rate of energy input, the authors documented unstable transition between bubbly and annular flow. Zhang et al. [3] also performed a flow visualization study of deionized water flow boiling in a parallel channel network and a single channel device. Flow oscillated between single and two-phase flow, a phenomenon attributed to pressure fluctuations. Wu and Cheng [4] investigated flow boiling of deionized water in two different microchannel heatsinks. Flow visualization showed oscillations between single and two-phase flow. Corresponding large amplitude, long period fluctuations in temperature and pressure measurements were recorded. Qu and Mudawar [5] reported hydrodynamic instabilities in two-phase water flow through a parallel channel heatsink. Flow reversal traveling to the inlet plenum was recorded. Pressure drop oscillations were observed for flow that was not throttled upstream of the test device. When the upstream flow was throttled, mild parallel channel oscillations were documented. A review of two-phase microchannel flow studies like those discussed above, lead Bergles and Kandlikar [25] to conclude that two instabilities exist, upstream compressible volume and excursion instabilities. Throttling the flow at the inlet of each channel was proposed to eliminate these instabilities.

The heat transfer capabilities of two-phase flow are superior to that of single phase flow and the latent heating associated with the phase change can provide better temperature uniformity along the flow path. Void fractions are an inherent part of two-phase flow and are used to better understand flow boiling. It is for this reason that quantifying void fraction variations is an objective of this study.

2.2. Research Objectives

The focus of this parametric study is two-phase flow in the fractal-like branching geometry proposed by Pence and Enfield [13]. Parameters include inlet mass flow rate and power input. For a given heat flux, the mass flow rate is varied while inlet temperature is held constant.

High-speed, high-resolution imaging was used to document flow regimes. The images will be evaluated for statistical local and regional void fraction variations. Effects of the bifurcations on vapor flow will be evaluated and interactions between branching levels investigated. Results are to be used to validate the pressure drop predictions of a one-dimensional two-phase algorithm currently being developed at Oregon State University.

3. TEST DEVICE DESIGN AND MANUFACTURING

3.1. Test Device Design

Figure 3.1 provides a cross-sectional view of an ideal test piece. The device is composed of two disks, a bottom layer with the channel network chemically etched and a transparent cover. The working fluid enters the center of the device, and flows radially to exits located along the outer circumference. A constant heat flux applied to the bottom of the test device supplies energy to the flow. The high thermal resistance of the device top ideally prevents energy loss.

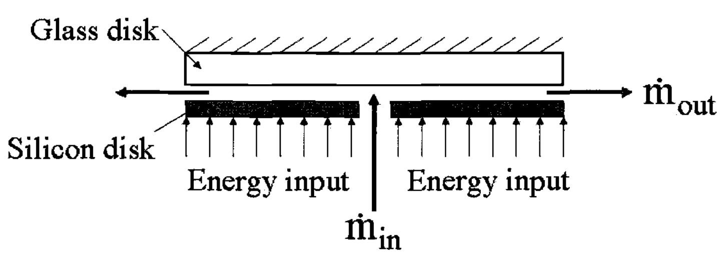

FIGURE 3.1. Cross-sectional view of an ideal test device.

An electric heater provides energy input to the flow. A uniform layer of resistive metal deposited on the bottom surface of the bottom disk of the test device forms the heater. A bottom disk with a large thermal conductivity theoretically should provide the desired maximum constant heat flux to the flow. In addition to having a thermally conductive bottom disk, the top disk ideally would be a perfect insulator.

The fluid in the test device is defined as the control volume for a global energy balance. A combination of sensible and latent heating of the flow increases the overall heat transfer rate, $\dot{Q}$.

$$\dot{Q} = \dot{m}_i C_p (T_{sat} - T_i) + \dot{m}_i x_e (h_g - h_f) \tag{3.1}$$

The quality at the test device exit, x_e, is defined as

$$x_e = \frac{m_v}{m_v + m_l} \tag{3.2}$$

Boundary conditions are based on the ideal test piece. The glass top is assumed a perfect insulator. By directly depositing heaters on the bottom of a highly conductive disk, a constant heat flux condition is assumed at this boundary. Flow exiting the test device is discharged into an open, annular plenum, therefore exit condition is assumed to be atmospheric pressure.

3.2. Test Device Manufacturing

The test device must allow two-phase flow in a fractal-like branching channel network to be visualized. The actual test device is based on the ideal test device design. The fractal-like pattern employed by this study is, for convenience, circular. The device is composed of two individual disks, one silicon and one Pyrex® glass. The disk materials were dictated by the thermal requirements discussed in Section 3.1, silicon has a thermal conductivity of 150 W/m K while glass is 1.5 W/m K, and by manufacturing specifications.

The fractal-like pattern was dry reactive ion etched (DRIE) 150 micron deep into a silicon wafer 38 mm in diameter and 500 micron thick. The resultant channel cross-section was not perfectly rectangular as hoped. Due to limitations in the etching process, the top of the channel is wider than the bottom. The channel dimensions are shown in Table 3.1. It should be noted that the reported lengths are based on radial distances and not actual channel lengths, see Fig. 3.2.

TABLE 3.1. Nominal channel dimensions.

k level	No	Depth (μm)	Width (μm)	D_h (μm)	Length (mm)
0	16	150	400	218	5.8
1	32	150	283	196	4.1
2	64	150	200	171	2.9
3	128	150	142	146	2.05
4	256	150	100	120	1.45

In addition, the hydraulic diameters are not based on a fixed ratio, but are the result of a fixed width ratio and a manufacturing dictated fixed depth.

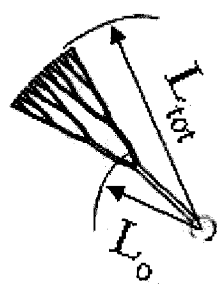

FIGURE 3.2. Lengths are radial distances.

A Pyrex® glass disk, 38 mm in diameter and 500 micron thick, was anodically bonded to the silicon disk forming the fourth wall of the channels. This optically transparent disk allows flow visualization. It should be noted that during the bonding process the glass was scratched. In addition, the glass and silicon disks were not perfectly aligned leaving small portions of some k = 4 level channels uncovered.

Following the bonding process, a passivation layer was grown on the non-channel side of the silicon wafer. A layer of nichrome, 5000 Å thick, was then deposited on the disk in the ring-like pattern shown in Fig. 3.3. The resistivity of nichrome is 0.0001 Ω·cm. The nichrome rings function as heaters when an electrical current is passed through them. An electrical insulator was deposited on top of the rings, but small contact pads were not insulated allowing electrical contact with each ring to be made. This particular pattern allows each of the first four branching levels to be heated individually.

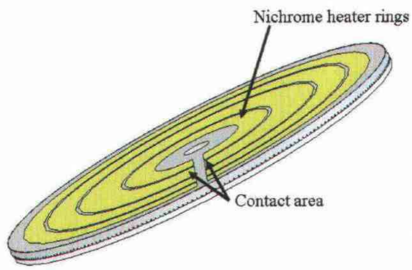

FIGURE 3.3. Nichrome heaters located on bottom side of test device.

4. EXPERIMENTAL FACILITY AND TEST PLAN

4.1. Manifold

A manifold was designed to act as an interface between the test device and flow loop. The manifold provides inlet pressure and temperature measurements, holds the test device firmly in place without obstructing the view of the flow, supplies a current to the resistance heaters on the backside of the test device, and prevents any leaking at the inlet or outer radius of the disk.

The manifold body, shown in Fig. 4.1, was machined from polyetheretherketone (PEEK). PEEK is an electrical and thermal insulator with excellent tensile strength at higher temperatures. Inlet pressure and temperature ports were machined in the manifold, 6.96 cm from the test device inlet. The large thermal resistance of the PEEK minimized thermal losses between the inlet measurements and the actual inlet to the test piece.

To hold the test device securely in place without obstructing the view of the flow or breaking the delicate test device, the manifold was designed to function as a vacuum chuck. A vacuum pulled through four holes, 1.6 mm in diameter, machined equidistant apart in the manifold top surface, holds the bottom surface of the test device securely against two silicon O-rings, resting in o-ring grooves also machined in the surface. The O-rings, located near the inner and outer radii of the test device, prevent leaking.

An additional set of holes, 0.94 mm in diameter, were machined into the top surface of the manifold and gold pogo pins were press fit into them. The contact pads of the nichrome heaters located on the bottom of the test device make electrical contact with the pogo pins when the vacuum is applied. A current is supplied to each heater via a pair of pogo pins.

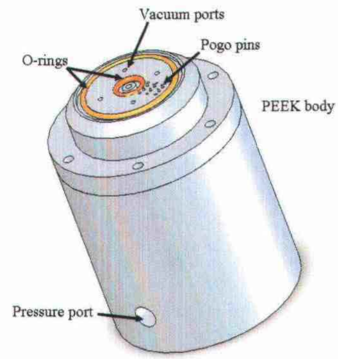

FIGURE 4.1. Manifold.

4.2. Flow Loop and Instrumentation

4.2.1. Flow Loop

A flow loop, shown in Fig. 4.2, provides a preheated working fluid to the test device. The working fluid is heated from room temperature to 80°C in a Vanguard 2000 W, 6 gallon water heater. The warmed flow is passed through a Shelco 10 μm filter and driven at a constant flow rate through the flow loop by a Micropump gear pump capable of 150 g/min at 75 psi. The pump is controlled with a manufacturer supplied rheostat. Two needle valves and a bypass line provide secondary flow control if necessary. The tubing is Swagelok one-quarter inch outer diameter, copper or stainless steel. Just before the test device, one-quarter inch, teflon tubing was used to minimize thermal losses and vibrations.

This is a closed flow loop, beginning and ending at the water heater. Heating of the flow occurs in stages. The working fluid exits the water heater at 80°C, a temperature that is maintained by an Omega iSeries controller with an accuracy of 0.02°C and a T-type thermocouple. Additional energy is added to the flow in a Neslab 800 W constant temperature bath ensuring the fluid leaves at the desired inlet temperature. The flow travels through another 0.6 m of tubing before entering the test device, and although the tubing is well insulated, losses do occur. Therefore, the inlet temperature is fine-tuned using a high temperature, 100 W, McMaster high temperature rope heater located just upstream of the test device inlet. The power output of the rope heater is controlled with a variac and adjusted manually to maintain a constant inlet temperature, measured at the manifold temperature port. Additional energy was added to the flow by resistance heaters on the bottom of the test device. DC constant voltage power supplies powered the heaters.

Upstream of the test device a Micromotion Coriolis mass flow meter, with a flow range of 0 to 1370 g/min and an accuracy equal to 0.10% of the rate, measures the inlet mass flow rate. Temperature and pressure ports located in the test manifold allow the inlet temperature and pressure to be measured 6.96 cm from the test device inlet. The temperature is measured with a Therm-X, metal sheathed, 4 wire, resistance temperature detector (RTD) with an accuracy of 0.7°C. A Cole-Parmer capacitance pressure transducer is used to measure the inlet pressure with an accuracy of 0.033 psig.

Liquid and vapor expel from the test device, and the liquid phase is captured in an annular plenum. A vacuum is applied to the plenum to remove vapor leaving the test device. The plenum was open to atmosphere, so the vacuum pulled was minimal, but necessary to prevent fogging of the imaging equipment. Downstream of the plenum, the mass flow rate of the working fluid is measured using another Micromotion Coriolis mass flow meter prior to being returned to the water heater.

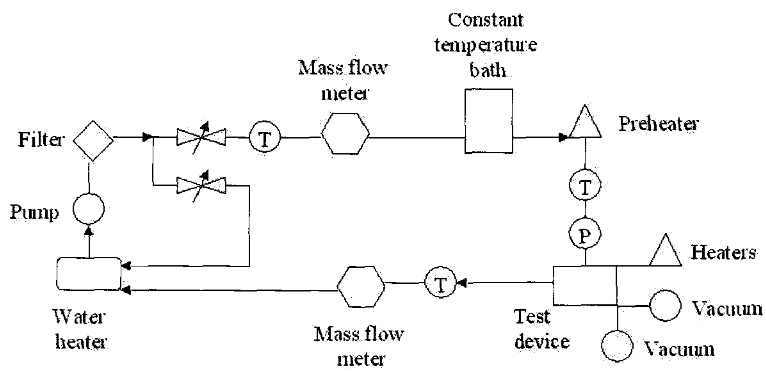

FIGURE 4.2. Flow loop.

4.2.2. Flow Visualization

Two-phase flow in the fractal-like branching channel network is recorded with a high-speed, high-resolution imaging system. The imaging set-up is shown in Fig. 4.3. A Nikon 60 mm f/2.8D AF Micro-Nikkor lens was used with a Vision Research Phantom v5.0 camera. The Phantom v5.0 recording speeds range from 60,000 fps at a resolution of 32 x 256 pixels to 1000 fps at 1024 x 1024 pixels. For this study 1000 fps adequately captured void fraction variations and provided a resolution of 630 pixels per cm. An exposure time of 10 μs was used. A Thor three-dimensional translation stage with 1.27 cm travel was used to adjust the camera position.

Rhodamine 6G dye was added to deionized, degassed water to create a solution with a molarity of 10^{-4}. The degassing procedure was accomplished by boiling the water for a thirty minute period in the water tank. A constant wavelength Coherent laser with wavelength of 532 nm was used to fluoresce the working fluid upon entering the test device. Rhodamine has a peak absorption at 532 nm wavelength laser light and peak emission at 550 nm, as shown in Fig. 4.4. A 570 nm long pass filter allows 60% of the emitted wavelength light to be imaged by the camera.

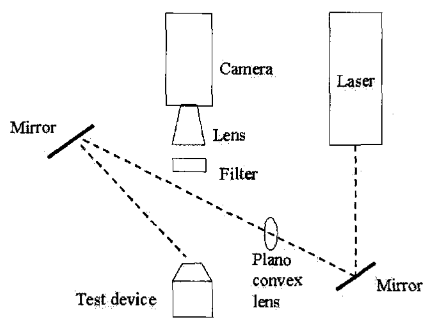

FIGURE 4.3. Flow visualization loop.

4.2.3. Data Acquisition

Global measurements such as inlet pressure and temperature were output as voltages and sampled at 1000 samples per second using two 16 bit data acquisition (DAQ) boards. Every seven seconds, the mean of the 1000 data samples was calculated and recorded using LabVIEW software. A circuit was built to translate the current and voltage supplied to the resistance heaters to voltages that could be sampled by the DAQ at 1000 samples per second. The inlet mass flow rate was output as a frequency and recorded using LabVIEW.

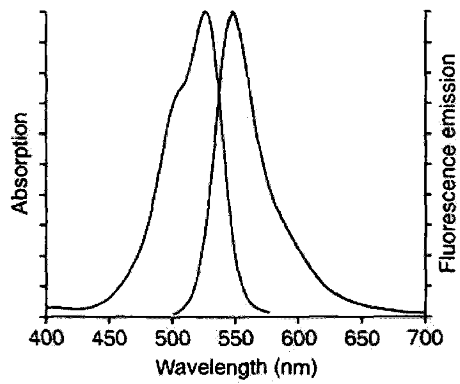

FIGURE 4.4. Rhodamine 6G absorption and fluorescence emission spectra from http://probes.invitrogen.com.

The Phantom v5.0 camera was controlled using the manufacturer supplied software. Images were stored in the volatile dynamic ram of the camera. Upon filling the camera memory, 1 GB, the images were extracted using the Phantom software and recorded in Cineon image file format for later conversion to bitmap format and image processing. The image data collection was not synchronized with the global data collection.

4.3. Test Plan

The test plan is based on the findings of related works and a battery of preliminary tests. A flow boiling investigation performed in a test device of similar composition to this study's test device with microchannels etched in a silicon bottom with an anodically bonded glass piece forming the top, showed that at higher flow rates the increase in pressure associated with phase change broke the silicon to glass bond [3]. These results were used to establish inlet mass flow rate and inlet pressure limits.

Recall that quality is the ratio of the vapor mass to the total mass of the fluid:

$$\mathrm{x} = \frac{\mathrm{m_v}}{\mathrm{m_v} + \mathrm{m_l}} \tag{4.1}$$

For even a low quality, because the density of liquid water is three orders of magnitude larger than that of water vapor, the vapor volume is large compared to the liquid volume. A sudden, significant change in vapor volume could break the test device, or produce dry out conditions. One the other hand, for this experiment to be successful, boiling must be visible. This goal must be balanced with the need to minimize vapor volume, placing additional constraints on the test plan.

Preliminary results also imposed limits on the rate of energy input and dictated a test procedure. A maximum energy input rate of sixty-six watts was set to prevent critical heat flux conditions and/or test device failure. Sixty-one watts represented the minimum energy input that would produce two-phase flow. In addition, it was determined it was most effective to start at a given heat flux and the fastest flow rate, and then incrementally decrease the flow rate. By decreasing the mass flow rate for a given energy input, the amount of boiling was increased slowly. This methodology ensured that if dry-out or test device breakage were to occur it would be at the end of an experiment rather than the beginning. The resultant test matrix is shown in Table 4.1.

The required camera frame rate and movie length were dictated by analysis of initial results. Preliminary movies taken at a frame rate of 1000 fps and shutter speed of 10 microseconds allowed the movement of bubbles and the vapor/liquid

TABLE 4.1. Test matrix.

	61 W	**66 W**
45 g/min	X (Case 1)	X (Base Case)
50 g/min	X	X (Case 2)
55 g/min	X	X
60 g/min	X	X
65 g/min	X	X

interface to be clearly visualized. A geometry of 1024 x 1024 pixels allowed one quarter of the test device to be imaged. Movies recorded using this geometry were one second in length due to camera memory limitation of 1 GB. The time period of a one second movie was not long enough to draw conclusions about the flow characteristics. Decreasing the geometry to 512 x 512 pixels, flow from the inlet to the exit in more than one tree was visible and the movie length was increased to 4.076 seconds increasing the duration to four times that of the original.

4.4. Procedure

The same procedure was followed for every test to ensure consistent results. Prior to each experiment the empty water heater was filled with seven liters of deionized water. The water was vigorously boiled for a thirty minute period. After this degassing process, the remaining volume of water was measured and the appropriate amount of Rhodamine 6G added to the water to achieve a molarity of 10^{-4}. A sample containing both rhodamine and water was heated until it began to boil, the boiling point was measured and shown to be the same was that of water.

The first step of each experiment was to warm the flow loop. This process began by heating the fluid in the water tank to 80°C. At the same time, the constant temperature bath was brought to 90°C. When these tasks were complete, the warmed fluid was pumped through the system at 100 g/min, bypassing the manifold and test device. The mass flow meters, the largest heat sinks in the loop, were warmed using heat blankets rather than waiting the hours required for the flow to bring them to temperature. When the fluid passing through the mass flow meters reached 70°C, the warm-up procedure was complete. The desired flow rate was set and flow sent to the manifold and test device.

At this point, the camera was positioned and the test device illuminated. Images of the fractal full of liquid were recorded. These base images were required for data analysis, which are discussed in Chapter 5. The inlet temperature of the fluid was then increased to the desired level by adjusting the power output of the rope heater located just upstream of the inlet. There is an order of magnitude difference between the coefficient of thermal expansion of silicon and that of glass; therefore, the test device heat flux was incrementally increased to the desired level.

When the inlet mass flow rate of two-phase flow and the energy input were constant for thirty minutes, the experiment was considered steady-state. Once the experiment was steady-state, ten movies were recorded over the next thirty minutes. Each movie had an image size of 512 x 512 pixels, a shutter speed of 10 microseconds, and a frame rate of 1000 fps. Transferring a movie from the camera memory to the computer took approximately three minutes. The time period associated with this transfer and an experiment length of thirty minutes dictated that ten movies could be recorded per experiment.

After ten movies for a particular flow rate and power were recorded, the flow rate was decreased by 5 g/min and the imaging procedure repeated. The flow rate was decreased a total of four times while the power was held constant. After the fifth experiment was finished, the shut down procedure was implemented. The power was then decreased incrementally, again to avoid thermal mismatch, until the test device was no longer heated. At this point, all heaters were turned off and the flow gradually slowed to a stop. The test device was flushed with deionized water to prevent the Rhodamine 6g from staining the silicon and the flow loop was shut down.

5. DATA REDUCTION AND ANALYSIS

5.1. Data Reduction

5.1.1. Global Data Reduction

Global measurements of pressure, temperature, mass flow rate, and energy input quantify the inlet conditions of each experiment. All inlet measurements were made for the duration of the steady state experiment. The instrument outputs were sampled at 1000 samples per second, and the mean of the 1000 data samples was calculated. The mean was recorded, writing the data to an output file took 7 seconds, after which another 1000 samples were measured and the process repeated. The voltage output of the pressure transducer and RTD were converted to pressures and temperatures using the calibration equations shown in APPENDIX A. The inlet mass flow rate measurements were converted from frequencies to flow rates using a linear relationship, APPENDIX A.

A circuit translated the currents and voltages supplied to the resistance heaters into voltages, V_I and V_V, respectively, that could be measured by the DAQ. The voltage drop measured across a current sense resistor was used to calculate the current, I, supplied to the heater, Eq. 5.1. The voltage supplied to the heater was too large to be read by the DAQ and was sent through a voltage divider before being measured. The actual voltage supplied to the heater, V, was calculated using Eq. 5.2. The calculated current and voltage values were used to determine the nominal rate of heat transfer. Once corrected for thermal losses, q_{losses}, the actual heat transfer rate, q, is calculated using Eq. 5.3. Thermal losses include conduction from the test device bottom to the manifold and radiation and convection from the test device top. Conduction losses from the test device bottom to the manifold were neglected because the thermal conductivity of PEEK, the manifold material, is 160 times smaller than that of silicon. Losses due to convection and radiation were estimated to be 2 W, about 3% of the maximum energy input.

$$I = \frac{V_I}{R_{sense}} \tag{5.1}$$

$$V = V_v * \frac{R_{10M\Omega}}{R_{10M\Omega} + R_{470k\Omega}} \tag{5.2}$$

$$q = (V * I) - q_{losses} \tag{5.3}$$

A constant heat flux boundary condition was assumed at the bottom of the test device. Several possible heat transfer areas exist. The area of the device bottom, where the heaters are located, is 11.4 cm^2. This area was used to determine the heat flux applied to the flow. It should be noted that, the four heater rings deposited on the bottom of the test device cover 8.3 cm^2 of the available 11.4 cm^2. An O-ring at the outer diameter of the test device prevents the fourth heater ring from being used, decreasing the heater area to 6.15 cm^2. In addition, the convective surface area is 5 cm^2.

Two other factors affecting the constant heat flux boundary should be noted. The $k = 4$ level does not have a heater ring directly below it, as the other branching levels do, and relies on conduction for its energy input. An o-ring at the inlet of the test device causes pooling of hot water in the area between the o-ring and the inlet plenum potentially increasing the temperature of the disk in this area. Despite these issues, because of the high thermal conductivity of the silicon, 150 W/m K, the constant heat flux boundary is considered a safe assumption.

5.1.2. Regional and Local Data Reduction

Regional and local data were analyzed for variations in void fraction. The void fraction was calculated directly from the image data, but the raw images were processed first using the MATLAB Image Processing Toolbox. This package uses algorithms, that can be used as supplied or modified by the user, to enhance and analyze images. The first image processing step was to adjust the image contrast. A shutter speed of 10 μsec resulted in dark pictures despite the use of a laser and fluorescent dye to illuminate the flow. This contrast adjust was achieved using a MATLAB algorithm that remaps the intensity values of the grayscale image based on a measurement of the high and low intensity values of the original image. The contrast adjusted grey threshold image was then converted to black and white format. The void fraction calculation, discussed in the following paragraphs, required binary images. The MATLAB programs used are located in APPENDIX B.

As was mentioned previously, both regional and local data were analyzed. A region includes the entire channel less the bifurcation areas. Regions in the k = 2 branching level, shown in Fig. 5.1, are defined as follows. In the area of interest, two isosceles triangles were defined. Triangle one is located at the upstream bifurcation, outlined in blue. A second triangle was placed at the downstream bifurcation of one of the channels emanating from the upstream bifurcation, outlined in green. The regions between the triangles were connected, the leg of triangle one to the base of triangle two, to form channel regions which are outlined in red. The same methodology was employed when defining the regions of the k = 3 level.

Void fraction, α_{vol}, is defined in terms of volume,

$$\alpha_{\text{vol}} = \frac{V_g}{V_g + V_f} \tag{5.4}$$

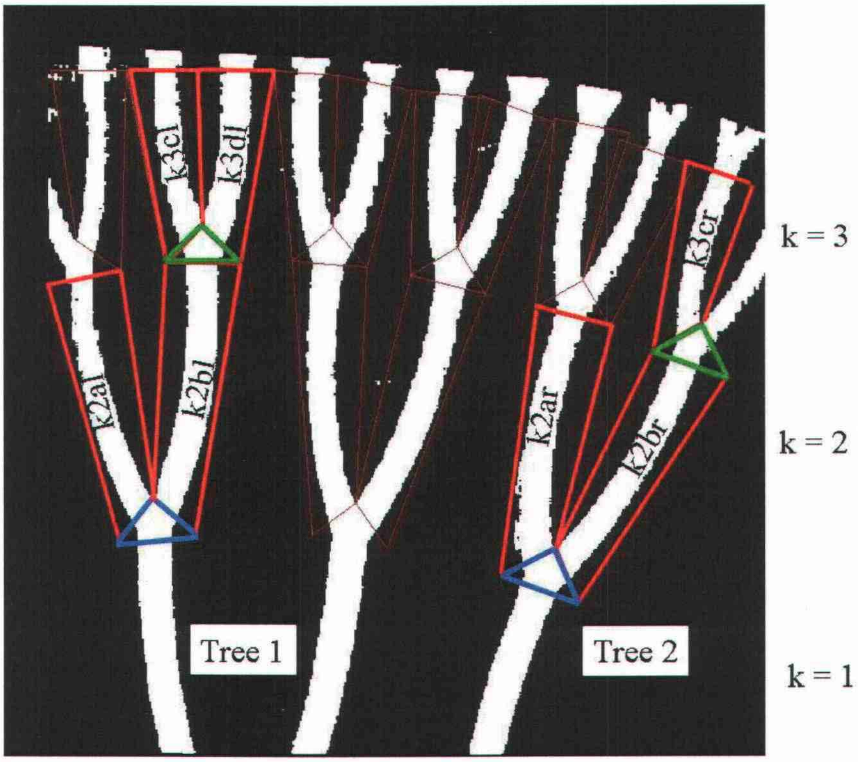

FIGURE 5.1. Regions of interest located in the k = 2 level.

In this experiment, all void fraction data were recorded as images. Because the images are two-dimensional, an apparent void fraction was defined. The regional void fraction calculation began with a black and white image of a fractal full of liquid, the base image. In the binarized images liquid appeared white while any vapor was black. The number of white pixels in a region of this base image were counted. Then the number of white pixels in the same region of a data image, one in which there was two-phase flow, were counted. The regional void fraction was calculated by subtracting the data image white pixel count, $\mathrm{NWP_d}$, from the base image count, $\mathrm{NWP_b}$, and normalizing with the base image count,

$$\alpha = 1 - \frac{\mathrm{NWP_d}}{\mathrm{NWP_b}} \tag{5.5}$$

Once the void fraction of the same region of every image of a given movie was quantified, these values were summed, and then divided by the total number of images in that particular movie, providing the time averaged void fraction. Because the regional void fraction was calculated for every frame of a movie a time series analysis could also be performed using these values.

In addition to regional void fractions, local void fractions were also measured. The bifurcations were the focal point of the local study. The three sides of the triangles of the regional study defined locations of interest. The side walls of the triangle were considered the right and left exits of a bifurcation. The base of the triangle formed the bifurcation entrance. The same methodology for calculating regional void fraction was employed for local calculations, with a line replacing a region. The line cuts across the channel, perpendicular to the channel wall. A line is essentially a one-dimensional region and, therefore, local void fraction calculations were the same as those performed in the regional study. The number of white pixels in a 1-D region of the data image are counted and subtracted from the base image white pixel count for that region.

5.1.3. Uncertainty

Instrument error was determined using the root square sum (RSS) method [26]. The inlet temperature measurement, made with a Therm-X metal-sheathed RTD with a range of -50°C to 260°C, had a calibrated uncertainty of $\pm$0.14°C. The RTD was calibrated using an Omega PCL-1B calibration unit and the Omega PCL-MR-1 temperature module, which had a range of 400 Ω. Inlet pressure measurements made with a Cole Parmer capacitance pressure gage, with a range of 0 to 25 psig, have an uncertainty of $\pm$0.02 psig. The pressure trans-

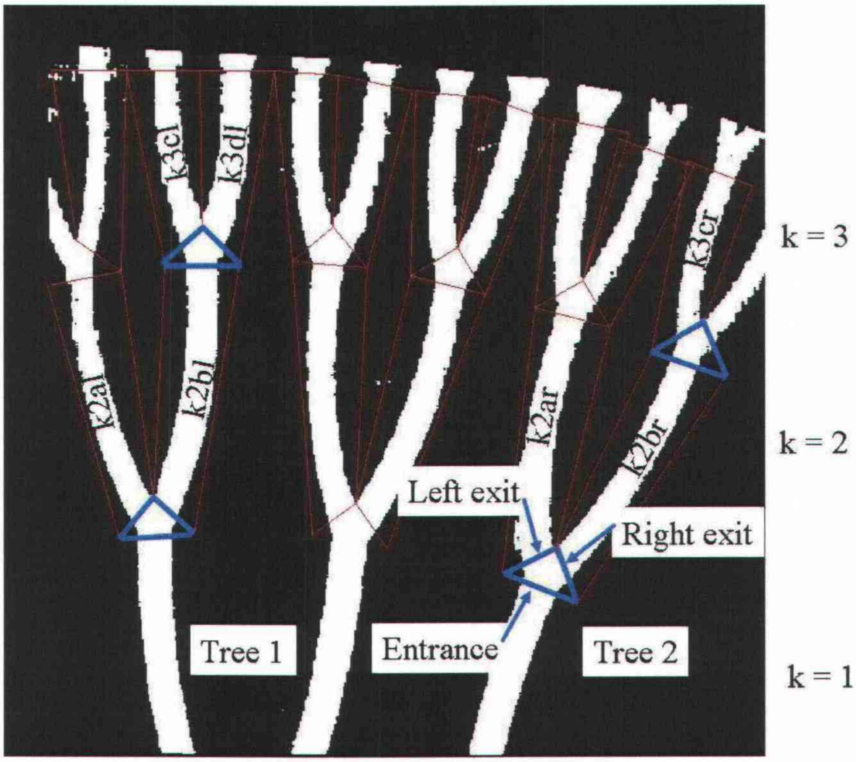

FIGURE 5.2. Definitions associated with the local study.

ducer was calibrated using an Omega PCL-1B calibration unit and the Omega PCL-MB pressure module, which has a range of 0 to 100 psia. The mass flow rate was measured using a Micromotion Coriolis mass flow meter, with a range of 0 to 1370 g/min. The mass flow measurements had a manufacturer specified uncertainty of $\pm$0.045 g/min.

As was mentioned in Chapter 4, a circuit was built to translate the current and voltage supplied to the resistance heaters to voltages, V_I and V_V, that could be sampled by the DAQ. The power supplied by the heaters was calculated from these voltages. Using the RSS method the uncertainty of this calculation was determined to be $\pm$3.6 W.

A sensitivity analysis was performed to determine the affects of image processing on the void fraction calculation. Adjusting the image contrast and threshold and binarizing the image results in an uncertainty of 1%.

5.2. Data Analysis

The high-speed, high-resolution images were reduced in four different ways; time-averaged and instantaneous regional void fractions as well as local time-averaged and instantaneous void fractions resulted. Time-averaged, regional void fraction data were analyzed for trends, in particular an increase with time, which often indicates flow instabilities. The instantaneous void fraction data associated with each time-averaged data point was then evaluated for a clearer understanding of the physical mechanisms at work. For example, if two regional, time-averaged void fractions from the same test were very different, their instantaneous data was analyzed for an explanation. Likewise, if two regional, time-averaged void fractions from the same test had the same magnitude, their instantaneous data were evaluated to see if their behavior was truly the same or if some detail was being lost in the averaging process. Local void fraction data were analyzed in the same manner.

6. RESULTS

Ten cases were investigated in this parametric study. Five different flow rates for two different energy inputs were examined. A base case was decided upon and analyzed. The base-case operating conditions included a power input of 66 W, flow rate of 45 g/min, and an inlet temperature of 88°C. As was mentioned in Chapter 4, this temperature measurement was made at a location in the manifold 6.96 cm below the test device inlet. The results of the base case are discussed in this chapter and compared to case 1 and case 2. The first comparison case, case 1, has the same inlet temperature and flow rate, but a lower power input of 61 W. The second comparison case, case 2, has the same inlet temperature and energy input, but the flow rate is increased to 50 g/min.

The same nomenclature is used when discussing the results of each case. A tree was defined in Chapter 1 as being composed of all the channels emanating from a particular k = 0 level channel. The camera settings used in this experiment, and discussed in Chapter 4, capture portions of two trees of the fractal-like pattern shown in Fig. 6.1. The tree to the left of the image is referred to as tree 1 and tree 2 is located on the right-hand side of the image. The regional analysis focuses on the k = 2 and k = 3 levels of these two trees. The regions, outlined in red in Fig. 6.1, encompass all of the channel except the bifurcation. Each region is given a name related to its tree, level, and location within the level. For example, region k3br is located in the k = 3 level, 'k3', the branches of the each level are labeled alphabetically and this is the second region of tree 2, 'b', and tree 2 is on the right-hand side of the image, 'r'. All results are discussed using these terms. The qualitative results are discussed first followed by an in depth quantitative analysis.

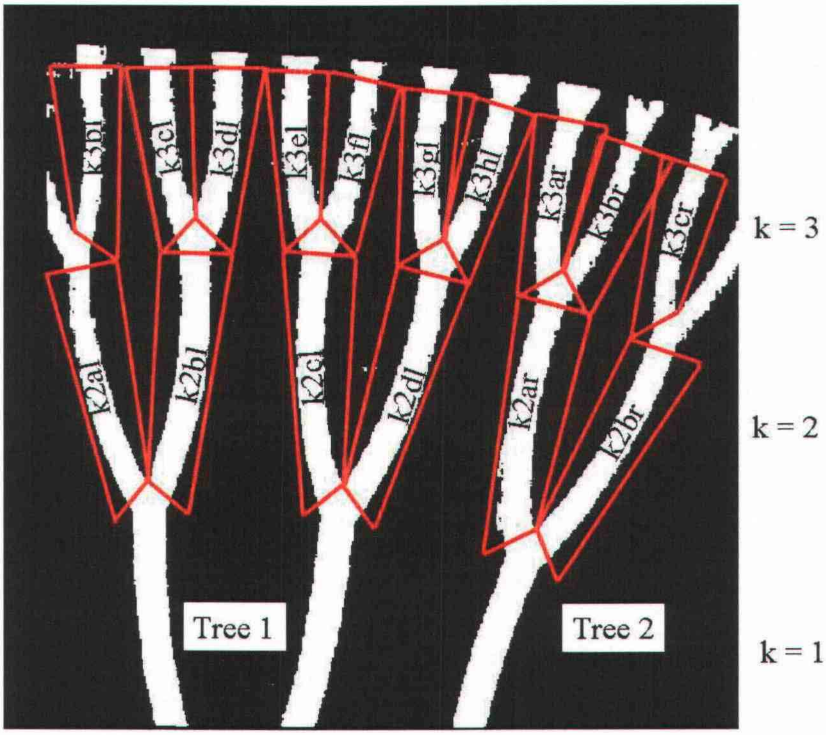

FIGURE 6.1. Definitions and key terms used when discussing results.

6.1. Qualitative results

The base-case (q = 66 W, ṁ = 45 g/min, and T_i = 88°C) movies were initially evaluated from a qualitative standpoint. Both levels of tree 2 were examined, beginning with the k = 2 level. Tree 1 had void fraction changes for three out of the ten movies, while tree 2 displayed significant void activity in nine out of the ten movies. Tree 2 experienced time variations in void fraction during the three movies in which tree 1 also displayed changes. The flow regimes observed in this branching level include single phase and slug flow, examples of which are shown in Fig. 6.2. For a given region, if a small portion of the channel is liquid flow and the remainder is vapor flow, it is defined as slug flow. The flow regimes observed at any instant in time varied from channel to channel in the this k = 2 level.

Prior to converting data images of the flow to binary format, liquid flow is white while vapor shows up as shades of gray. Vapor flow in this level often does not have a clearly defined outline, appearing more like a gray front moving through the channel, as shown in Fig. 6.2. Typically, vapor originating in the k = 2 level moves downstream towards the outer radius of the test device, but on occasion the vapor flows upstream from the k = 3 level towards the inlet plenum through the k = 2 level.

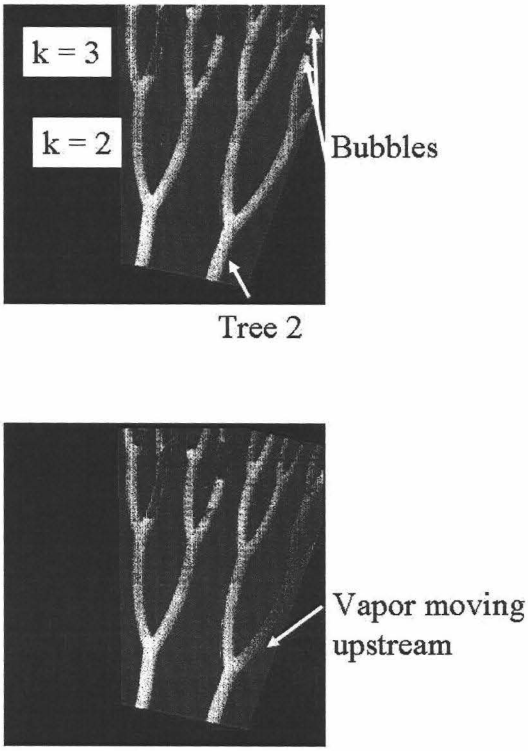

FIGURE 6.2. Four images 0.005 seconds apart from a base-case movie that demonstrate the observed bubbles, slugs, and vapor fronts.

In the k = 3 level regions, the base-case qualitative results show that both tree 1 and tree 2 experience void fraction variations in all ten movies. The flow is a combination of single phase, bubbly, and slug flow. Vapor in the k = 3 level region of tree 1 results from bubbles in the k = 4 level growing upstream. Tree 2 has significant bubble growth on the k = 3 level and also experiences vapor fronts like those described when discussing the k = 2 level qualitative results.

The ten base-case movies were evaluated qualitatively. The k = 2 level was observed to experience periods of single phase flow and instances of slug flow. The k = 2 level of tree 2 is more active than the same level of tree 1. This is most likely due to tree 2 having a larger number of observed nucleation sites. Single phase, bubbly, and slug flow were recorded in the k = 3 level. These qualitative findings were used to define the quantitative study that follows.

6.2. Quantitative Results

The base case discussed in Section 6.1 will be analyzed from a quantitative standpoint. The base-case results are compared against those of two other cases. Base-case operating conditions include a power of 66 W, mass flow rate of 45 g/min, and inlet temperature of 88°C. Case 1 uses the same mass flow rate and inlet temperature, but the power level is decreased to 61 W. In case 2, the power and inlet temperature is the same as the base case, but the mass flow rate is faster at 50 g/min. The results are first examined regionally. The regions of interest were defined in Chapter 5 to encompass the entire channel length except the area surrounding the bifurcation. Both time-averaged and instantaneous regional results are reported. The results are then evaluated locally. Time-averaged and instantaneous void fractions are evaluated at specific streamwise locations represented by lines that span the width of the channel and are perpendicular to the channel wall.

6.2.1. Base-Case Regional Quantitative Results

Global measurements of energy input, inlet pressure, temperature, and mass flow rate were sampled at 1000 Hz during a thirty minute period. Every seven seconds, the mean of the 1000 data samples was calculated and recorded. Recording the mean of the measurement, rather than the instantaneous data, with too slow a sample rate prevented the observation of high frequency pressure oscillations noted in other studies [23, 24, 25]. A summary of the base-case global data is shown in Fig. 6.3. Again, the nominal base case operating conditions included a power input of 66 W, mass flow rate of 45 g/min, and inlet temperature of 88°C. The average power input was calculated to be 65.9 W with a standard deviation of 3.6 W, and the standard deviation of the averaged values equal to 0.24 W. The mean inlet pressure was determined to be 0.86 psig with a standard deviation of 0.017 psig and a standard deviation of the averaged values equal to 0.001 psig. The average inlet mass flow rate was 44.79 g/min and the standard deviation of the mean calculated to be 0.003 g/min. There was a 2% change in the inlet mass flow rate at t = 12 min, due to a manual adjustment of the flow rate at this time. The average inlet temperature was calculated to be 87.7°C with a standard deviation of 0.003°C and a standard deviation of the mean equal to 0.0002°C.

Each movie was 4.075 seconds in length and composed of 4075 frames. The void fraction for every region in each frame was calculated using the methodology described in Chapter 5. The 4075 void fractions of a particular region were averaged over 4.075 seconds, resulting in the time-averaged data for that particular region. This process was performed simultaneously for all fourteen regions, highlighted in Fig. 6.1. It should be noted that a total of ten movies were recorded

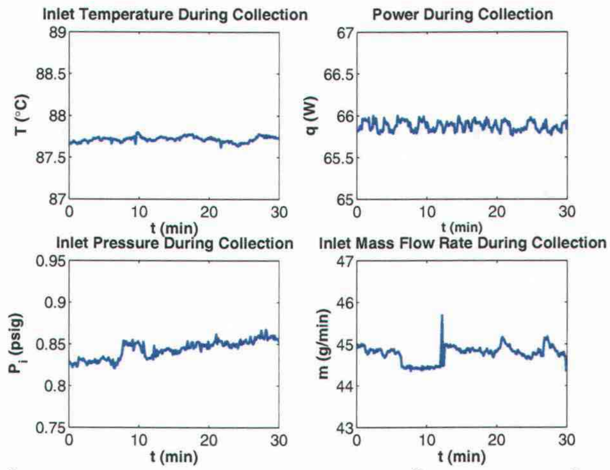

FIGURE 6.3. Inlet temperature, pressure, mass flow rate, and power input measurements sampled at 1000 Hz, the mean of which was recorded every seven seconds for the thirty minute period.

during the thirty minute period. Whenever possible the movies were taken every three minutes. On occasion the camera lens would become fogged, extending the three minute interval.

The base-case, regional, time-averaged data of the k = 2 level of tree 2 will be evaluated first. Instantaneous data for the regions of this level will be used to explain the time-averaged findings. A study of the k = 3 level regions of tree 2 will follow, with time-averaged data followed by instantaneous analysis. Finally the tree 2 data will be compared with that of tree 1.

Figure 6.4 shows the base-case, regional, time-averaged data associated with the k = 2 level of tree 2. With the exception of t = 14 min, the time-averaged void fraction was constant at approximately 0.1. The k2ar and k2br regions demonstrated symmetrical void fraction behavior with the void fraction magnitude of the k2ar region consistently smaller than that of the k2br region. These channels shared an upstream bifurcation as was seen in Fig. 6.1. Qualitative analysis showed vapor occupying the k = 3 level region often flowed upstream into the associated k = 2 level channel, the vapor continued moving upstream until it reached the k = 2 level upstream bifurcation. The vapor then hooked around the bifurcation and began moving downstream through the k = 2 level channel that shared the bifurcation with the channel containing the upstream moving vapor. Observations indicated that certain conditions, such as bubbles located in channels downstream of the channel of interest, were often associated with upstream vapor flow. The large resistance to the flow in the associated downstream channels, due to bubbles, may result in long vapor residence times in the channel upstream of the bubbles. The long residence time in this region could produce a larger magnitude void fraction in the channel with upstream vapor flow. In addition, the flow is noted to hook around the bifurcation and begin moving downstream again. The channels through which there is downstream vapor flow have less bubbles and, therefore, provide less resistance to the flow, providing an alternative downstream route and possibly preventing upstream flow instability.

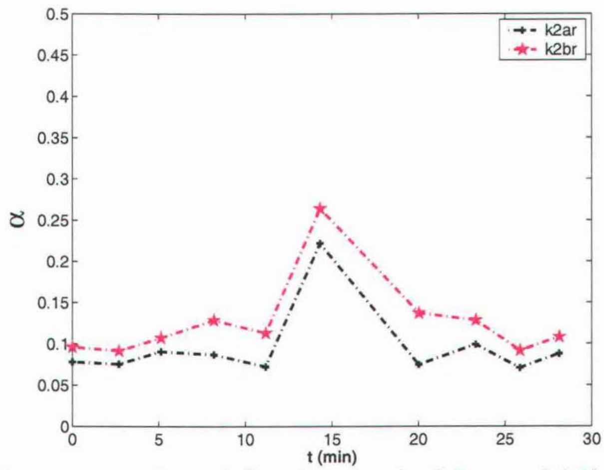

FIGURE 6.4. Time-averaged void fraction in the k2ar and k2br regions determined for each of the ten movies.

The movie from t = 14 min has a void fraction that is three times that of the other nine movies, as demonstrated in Fig. 6.4. A constant heat flux was applied to the device and uniform energy input assumed. The 2% change in mass flow rate noted at t = 12 min, seen in Fig. 6.3, potentially caused this difference. A time series analysis may help explain this anomaly.

The movie from t = 14 min demonstrated the largest time-averaged void fractions in the k = 2 level of tree 2 during the thirty minute evaluation period. The instantaneous data, shown in Fig. 6.5, indicates the channels experienced significant periods of void fraction. The regions examined filled quickly with vapor, indicated by a rapid increase in void fraction, that resided for periods spanning 0.1 to 0.5 seconds before being replaced with liquid. Several changes larger than 70% occurred in both regions during this four second interval. The void fraction changes in the k2ar and k2br channels followed the same pattern. This is most likely due to the fact that these channels shared an upstream bifurcation.

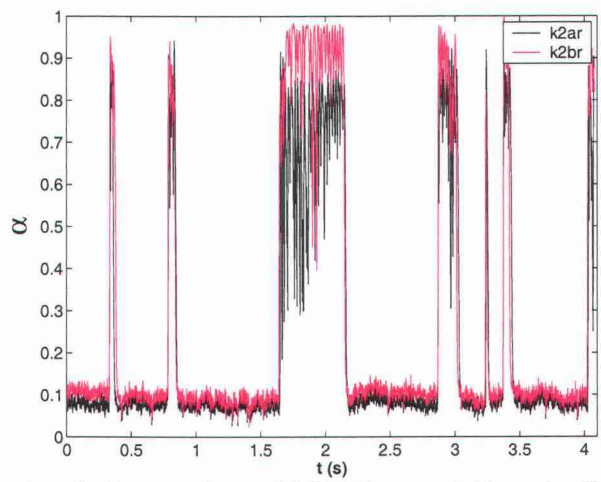

FIGURE 6.5. Regional, time series void fraction variations in the k = 2 level of tree 2, associated with t = 14 min movie.

A closer look at the time series data from the t = 14 min movie, presented in Fig. 6.6, shows fast oscillations occur when the average void fraction is greater than 0.6. The oscillations were 180° out of phase, with the void fraction in k2ar at a minimum when the k2br void fraction was at a maximum. There appears to be a frequency associated with these oscillations, requiring a power spectral density (PSD) analysis of the signal.

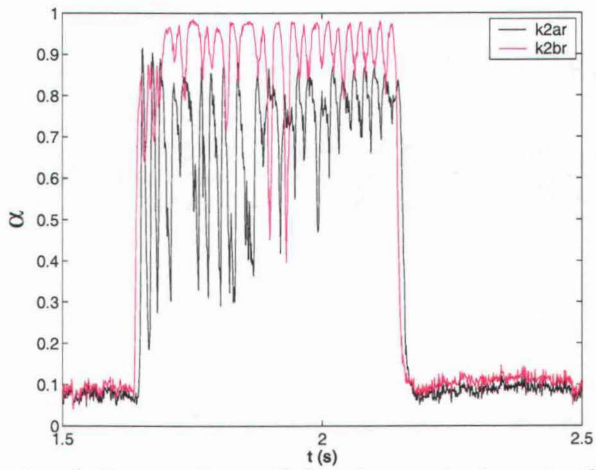

FIGURE 6.6. Regional, time series void fraction variations, in the k = 2 level of tree 2, associated with t = 14 min movie between t = 1.5 and 2.5 s.

A PSD analysis of the void fraction data from t = 1.5 s to t = 2.5 s of the t = 14 min movie was performed. The Welch averaged, estimated periodogram method was employed to make the PSD estimate. The signal, time series void fraction minus the mean void fraction, was divided into a predetermined number of segments with a 50% overlap. The segments were windowed using a Hamming window. PSD estimates for each segment were made and then averaged. Analysis of the void fraction in the k2ar and k2br regions of tree 2 during this time period indicates the oscillations occur at a frequency of 50 Hz.

As with the t = 14 min movie, the movie from t = 3 min represents an extreme case. The time-averaged void fraction of the t = 3 min movie was the smallest of the thirty minute period.

The void fraction in the k2ar and k2br regions was nearly constant for the duration of the movie recorded at t = 3 min, shown in Fig. 6.7. No activity was observed in these regions when the movies were visually evaluated. A void fraction of 0.08 suggests these particular regions were darker in the data images than the same regions in the base image. It is possible that bubbles were forming on the bottom of the channels, darkening the regions. It was also observed that the test device vibrated when two-phase flow passed through it and this motion could have affected the image processing and subsequent void fraction calculation.

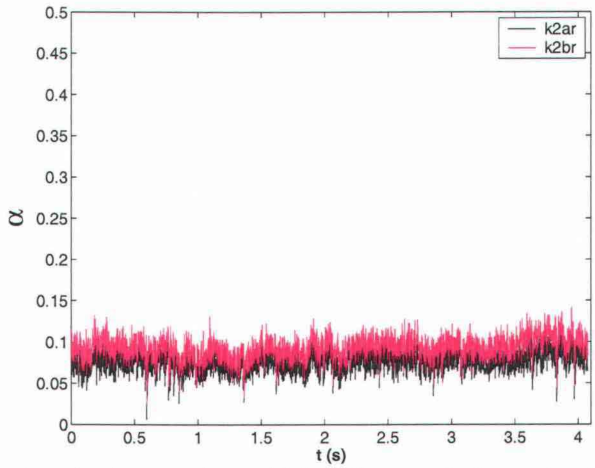

FIGURE 6.7. Regional, time series void fraction variations, in the k = 2 level of tree 2, associated with t = 3 min movie.

Channels with shared bifurcations on the k = 2 level appear to interact. The next step is to determine whether or not k = 2 level void fraction variations are affected by k = 3 level vapor. The k3cr region shares its upstream bifurcation with the k2br channel, as shown in Fig. 6.1. The t = 14 min movie instantaneous data of these regions are compared in Fig. 6.8. The k = 3 level demonstrated bubble growth, the void fraction increased from 0.1 to 0.5 between t = 2 s and t = 2.75 s, in addition to experiencing quick changes from all liquid to all vapor and back. The k = 2 level experienced these flashes of vapor just milliseconds after the k = 3 level. The activity of the downstream level affected the upstream level and vice versa.

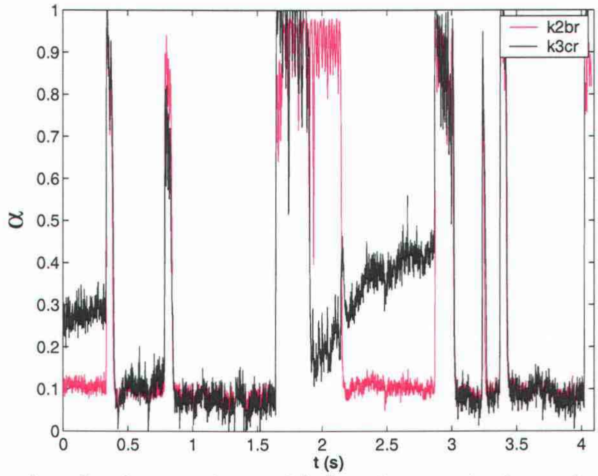

FIGURE 6.8. Regional, time series void fraction variations, in the k = 2 and k = 3 levels of tree 2, associated with t = 14 min movie.

Significant bubble growth was observed in the k3cr channel and in the k = 4 level channels downstream of it during the t = 14 min movie. The other k = 4 and k = 3 level channels of tree 2 had a void fraction near zero. Bubble growth in the k3cr channel and its associated k = 4 channels could be responsible for slowing liquid flow in these regions, allowing it to warm and evaporate. The blockage associated with bubble growth in these channels may result in vapor generation in the k2br region. An unblocked path to the test device exit, through the k2ar channel, allowed the vapor to begin moving downstream again. The bifurcation essentially redirected the vapor flow, most likely causing the similarly timed void fraction changes in channels sharing an upstream bifurcation.

The time series data evaluated represented two extremes within the base case, one where the time-averaged void fraction was at a minimum and the second when it was at a maximum. The instantaneous data associated with the minimum time-averaged void fraction, t = 3 min, did not accurately represent typical k = 2 level behavior for this case. Over 50% of the movies show the k = 2 level of tree 2 experienced moderate activity, with void fraction changes similar to those seen in the t = 14 min movie, shown in Fig. 6.5, but at a lower frequency. The time series data from the t = 14 min movie was evaluated for both the k = 2 and k = 3 levels. On the k = 2 level, several large changes in void fraction were observed. Interaction between the two levels was noted, and the k = 3 level demonstrated behavior not observed on the k = 2 level, requiring a further investigation.

Compared with time-averaged, base-case, tree 2, k = 2 data, the regional, time-averaged, base-case data for the k = 3 level of tree 2 varied significantly over the course of the thirty minute period, as seen in Fig. 6.9. The k = 3 level time-averaged void fractions measured at these times were larger than k = 2 level simultaneously calculated void fractions. This difference could be due to streamwise heating of the flow. The k3ar and k3br channels share an upstream bifurcation, as shown in Fig. 6.1, but these channels did not experience the similar changes in void fraction noted in k = 2 level channels with shared upstream bifurcations.

In most movies evaluated, the k = 4 level channels downstream of the k3ar region contained no bubbles. A lack of vapor in the k = 4 level appeared to lessen the potential of bubble formation in the k3ar channel, providing a possible explanation for the difference between k3ar and k3br time-averaged void fractions.

Qualitative analysis of the base-case movies show these two regions to have similarly located nucleation sites, near the k = 3 level upstream bifurcation, and comparable downstream, k = 4 level, activity.

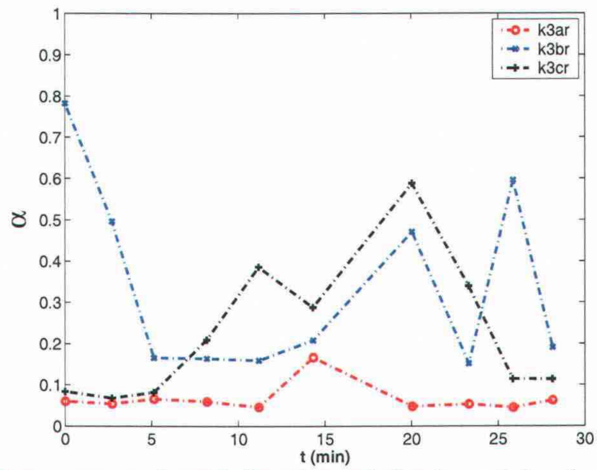

FIGURE 6.9. Time-averaged void fraction of the k = 3 level regions of tree 2 determined from each of the ten movies.

At t = 5 min, the time-averaged void fraction is small, less than 0.2, for all channels. At t = 20 min, the time-averaged void fraction is considered to be large, with values greater than 0.4 in two of the three channels. The time series data for times t = 5 min and t = 20 min are evaluated next.

The t = 5 min movie demonstrated the smallest time-averaged void fraction for the k = 3 level of tree 2 during the thirty minute evaluation period. The k3br and k3cr channels experienced one significant change in void over the course of four seconds, as shown in Fig. 6.10. The k3ar channel had a constant void fraction less than 0.1 for the entire movie and, therefore, was not plotted.

A closer look at the void fraction during the time period from t = 0.77 s to t = 0.88 s, as shown in Fig. 6.11, shows behavior similar to that seen on the k = 2 level in Fig. 6.6. The void fraction in the k3br and k3cr channels experienced rapid, nearly 180° out of phase, oscillations. A PSD analysis demonstrates that these oscillations occur at 70 Hz.

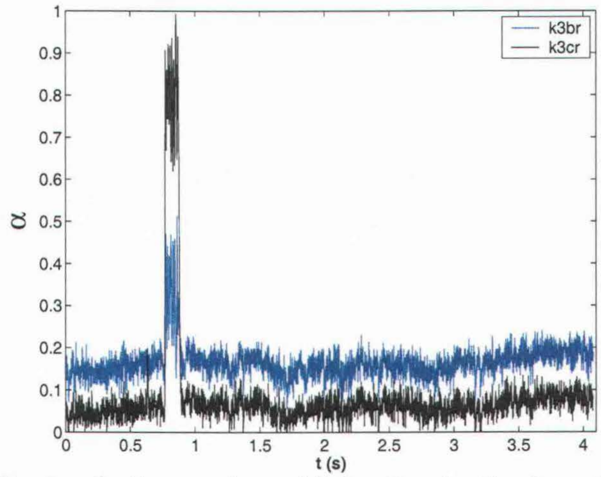

FIGURE 6.10. Regional, time series void fraction in the k = 3 level of tree 2 associated with t = 5 min movie.

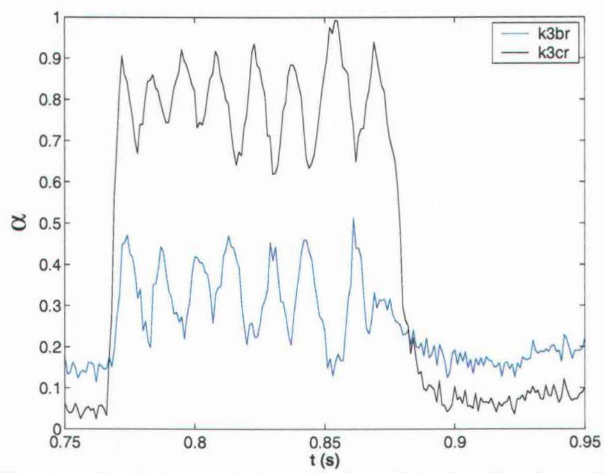

FIGURE 6.11. Regional, time series void fraction in the k = 3 level of tree 2 associated with t = 5 min movie when the average void fraction is large and the instantaneous void fraction oscillating.

Prior to the large increase in void fraction during the t = 5 min movie, the k = 4 level of tree 2 was observed to contain significant amounts of vapor.

Information about the $k = 4$ level void fraction is reported as observations only due to insufficient image resolution. In addition, both the k3br and k3cr channels demonstrated bubble growth. Liquid flow in the k3br and k3cr channels was blocked by vapor, which increased liquid residence time and in turn increased boiling in these $k = 3$ level channels. Some of the bubbles in the $k = 4$ level were pushed from the test device when the large vapor volume exited the test device at $t = 0.9$ s. The lack of bubbles blocking liquid flow is most likely why no more large changes in vapor occur.

The instantaneous data associated with the smallest time-averaged void fractions of this case, less than 0.2, demonstrated one large change in void fraction in each of the two channels evaluated. These channels share a bifurcation. This void fraction variation occurred in both channels, with one channel experiencing the change at a lesser magnitude a few microseconds after the other channel. A shared upstream bifurcation may be responsible for this similar void fraction change. Vapor in the $k = 4$ and $k = 3$ level channels, downstream of the $k = 2$ level regions evaluated, is noted to affect the flow in $k = 2$ level.

The $t = 20$ min movie represents the largest (four times greater than the $t = 5$ min case just evaluated), $k = 3$ level, time-averaged void fraction for the base case, as was seen in Fig. 6.9. Analysis of the associated instantaneous data may highlight differences between the two movies; time series data for the $t = 20$ min movie are shown in Fig. 6.12. Bubble growth, an increase in the void fraction from 0.5 to 1, in the $k = 3$ level was observed during the following time periods, $t = 0.1$ s to 1.0 s, $t = 1.3$ s to $t = 2.1$ s, and $t = 2.3$ s and $t = 3.\ 4$ s. This increase in void fraction affected the $k = 2$ level, as shown in Fig. 6.12(a). The k2ar and k2br channels share an upstream bifurcation, but did not demonstrate similar hydrodynamic behavior, seen in Fig. 6.12(b). Although k3br and k3cr do not share an upstream bifurcation, the relationship between these channels is shown in Fig. 6.1, both regions demonstrated an increase in void fraction from 0.5 to 1 between t = 0.1 s to 1.0 s and t = 1.3 s to t = 2.1 s, as seen in Fig. 6.12(c). The void fraction in k3ar was independent of the other two k = 3 level channels of this tree.

The k = 4 level channels downstream of k3br and k3cr were observed to be full of vapor during the t = 20 min movie. Bubble growth, a visible increase in bubble size, was noted in the k3br and k3cr regions. There was one path to the test device exit available to vapor generated in these regions; a k = 4 channel downstream from the k3ar region contained no vapor, allowing liquid flow to exit the test device and carry a portion of the vapor in the other channels of tree 2 with it. The void fraction in the k3cr region did not drop below 0.5 until the last 0.5 second of the movie, it is possible this was due to surface tension. At t = 1.28 s the surface tension force associated with a bubble located in the downstream portion of the k3cr region was calculated from the measured contact angle and bubble radius. This surface tension forces was compared to the inertia force associated with this channel and shown to be an order of magnitude larger. The inertia force was calculated using a measured velocity, the movement of a bubble front along a channel of known length provided this information, and k = 3 level mass flow rate.

During the t = 20 min movie, the k = 4 level conditions affected the void fraction in the k = 3 and k = 2 levels. Channels of the k = 3 level that did not share an upstream bifurcation still demonstrated similar hydrodynamic behavior. This was most likely due to the fact that k = 4 level channels downstream of the k = 3 level regions evaluated have similar vapor content. The k = 3 level regions that share an upstream bifurcation did not demonstrate the matching void fraction

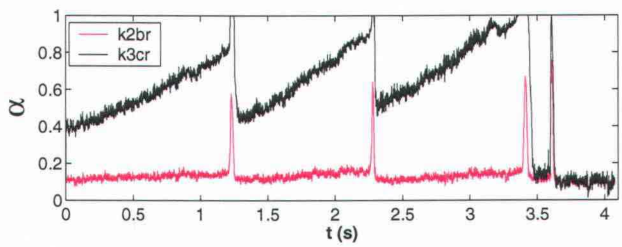

(a)

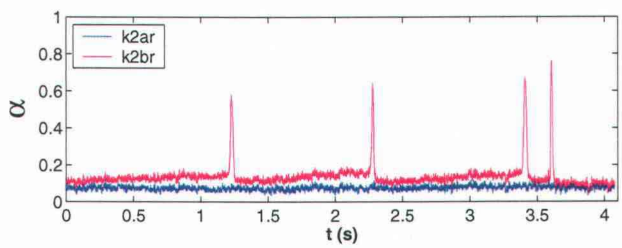

(b)

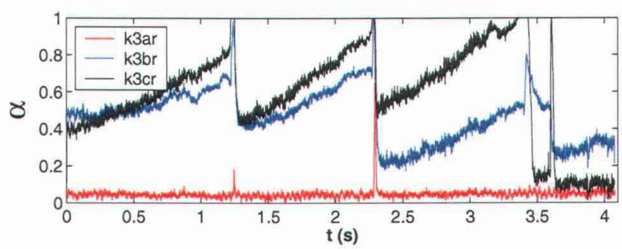

(c)

FIGURE 6.12. Void fraction variations in tree 2 during the t = 20 min movie. (a) Interaction between k = 3 and k = 2 levels. (b) No interaction on the k = 2 level (c) Similar behavior in the k = 3 level regions.

changes noted in k = 3 level channels sharing an upstream bifurcation in the t = 5 min movie. It has been proposed that the location of vapor in downstream channels affected flow in upstream levels during these movies. The bubble growth in the k = 4 and k = 3 levels during the t = 20 min movie, not seen in the t = 5 min movie, could explain the lack of symmetry in void fraction changes between channels sharing an upstream bifurcation in the t = 20 min movie. In addition, it appears that surface tension played an important role in flow behavior.

The time series data evaluated above represents two extremes within the k = 3 level of tree 2. The instantaneous data for the minimum and maximum time-averaged void fractions for this level were used to try to explain the difference between the two time-averaged values. An additional movie from this case, one that falls between the two extremes, was also evaluated. The time series data from t = 3 min movie is shown in Fig. 6.13. The k3br channel void fraction increased with time, growing from 0.2 to 1 between t = 0.6 s and 2.5 s. The k3cr channel void fraction was less than 0.1 until t = 3.6 s when the void fraction became five times larger.

Qualitative analysis of the t = 3 min movie showed a small amount of void to reside in the k3br channel at t = 0 s. The k = 4 channels downstream of the k3br channel were almost completely full of vapor. The vapor volume in the k3br region and its associated k = 4 level channels increased flow residence time, and promoted boiling. It is believed that the lack of activity in the k3cr region is explained by a lack of vapor in the k = 4 level downstream of this region.

Time-averaged and instantaneous void fraction data for both the k = 3 and k = 2 levels of tree 2 were evaluated. The k = 3 level was more active, with regions experiencing rapid changes from all liquid to all vapor and back. In addition, periods of bubble growth occurred on this level. Streamwise heating of

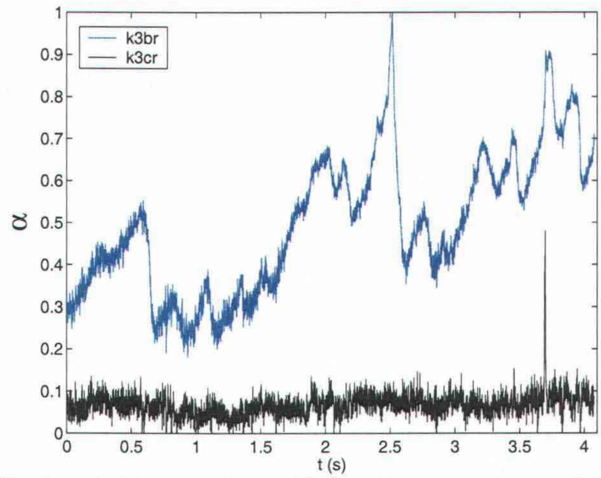

FIGURE 6.13. Regional, time series void fraction variations, in the k = 3 level of tree 2, associated with t = 3 min movie.

the flow may be responsible for greater activity in the k = 3 level. Interaction between levels was observed, the location and quantity of vapor in a particular channel or group of channels affected the regions downstream of it. During a period of lower void fraction activity, interchange between channels with shared bifurcations was noted. This interaction was not observed in a movie with more frequent void fraction variations. Surface tension forces in the k = 3 level appear to have affected flow behavior. The fractal-like device is composed of sixteen trees, therefore this evaluation of a single tree is not sufficient, and these results must be compared to those of another tree.

The regional, time-averaged and instantaneous void fraction data from tree 2 are now compared to that of tree 1, beginning with the k = 2 level. The tree 2 and tree 1 data were taken simultaneously. The regional, time-averaged void fractions of the k = 2 level of tree 1 were similar in magnitude to those of same level in tree 2, as shown in Fig. 6.14. Note, the relatively large change in void fraction observed at t = 14 min for the k = 2 level channels of tree 2 was not seen in tree 1. Previously it was suggested that a manual adjustment of the mass flow rate at t = 12 min may have caused the large, time-averaged void fraction in tree 2 at t = 14 min. Tree 1 did not experience the same jump in void fraction at t = 14 min, no longer lending support to this explanation.

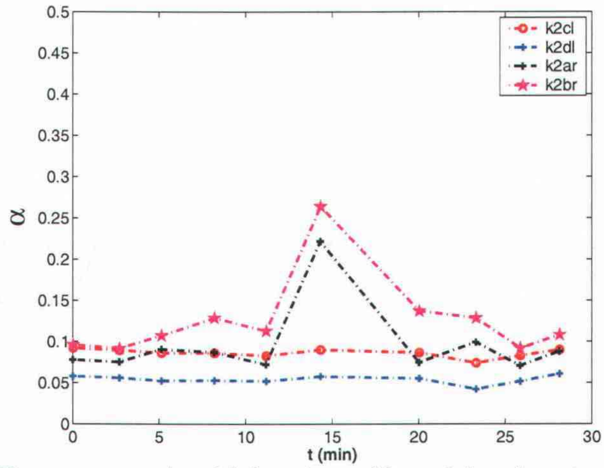

FIGURE 6.14. Time-averaged void fraction of k = 2 level regions of both tree 1 and 2 determined from each of the ten movies.

At t = 28 min, the time-averaged void fractions of the k = 2 level channels of both trees were essentially the same, as seen in Fig. 6.14. The instantaneous data at this time show both trees experienced a single, rapid change from all liquid to all vapor and back, in at least one channel within the level, as noted in Fig. 6.15. Although the k2cl and k2dl channels share an upstream bifurcation, the k2dl channel experienced a significant void change while the k2cl channel void fraction remained constant.

Observations made during the t = 28 min movie indicated the k = 4 level channels downstream of the k2cl and k2dl regions were full of vapor prior to the large increase in void fraction at t = 2.8 s. In addition, the k = 3 level region located downstream of the k2cl channel was also full of vapor. Qualitative analysis of the t = 28 min movie showed the vapor to originate at the k = 1 level. This vapor traveled downstream through the k2dl channel only. The vapor slug located in the k3fl channel, directly downstream of the k2cl region, is proposed as the reason for the preferential movement of vapor through the k2dl region. This behavior may be an indicator that flow moving downstream through a bifurcation will not be split evenly between the two downstream channels if there is vapor located downstream of that bifurcation.

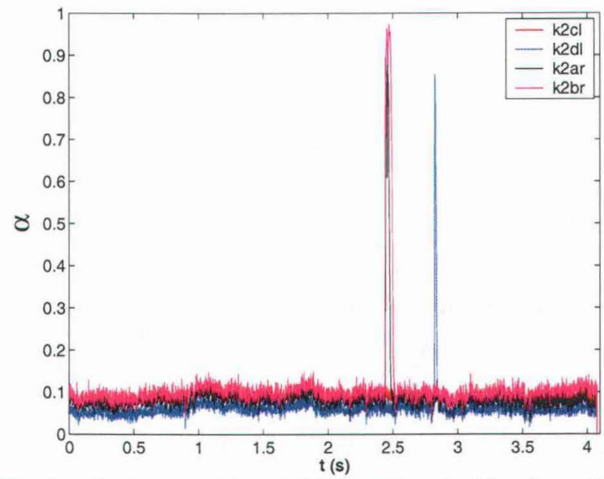

FIGURE 6.15. Regional, time series void fraction in the k = 2 level of trees 1 and 2 associated with t = 28 min movie.

On the k = 2 level, data taken simultaneously for the two trees indicated the behavior of each tree was independent of the other. In both trees, the k = 2 level void fraction was affected by downstream levels. The k = 3 level void fraction data of both trees are evaluated for further understanding.

The regional, time-averaged void fraction data for the k = 3 level of trees 1 and 2 are compared in Fig. 6.16. Changes in void fraction from movie to movie were larger in tree 2. In tree 1, the time-averaged void fraction of the k3fl channel was consistently larger than that of the k3gl region. During the k = 2 level evaluation of the t = 28 min movie, a slug was noted to reside in the k3fl region. Qualitative analysis of the base case movies showed this slug to reside in this channel for several of the movies, most likely causing the consistently larger time-averaged void fraction in this region.

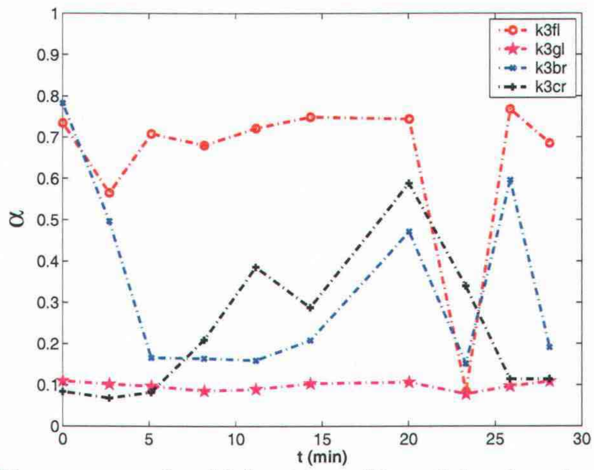

FIGURE 6.16. Time-averaged void fraction of k = 3 level regions of both tree 1 and 2 determined from each of the ten movies.

A bubble was observed to reside in the k3fl region, filling a portion of the region, for the entire t = 28 min movie. This kind of behavior has not yet been investigated, and will be done so now. A comparison of the time series void fraction data of the k = 3 levels of tree 1 and 2 is shown in Fig. 6.17. The k3fl region of tree 1 contained a growing bubble, the void fraction increased from 0.5 to 0.8, and the bubble oscillated, changed size, over the course of the movie. The channel sharing an upstream bifurcation with k3fl, k3gl, had a constant void fraction of approximately 0.1 for almost the entire movie. The k3gl region experienced one rapid change from all liquid to all vapor and back at t = 2.8 s. Unlike tree 1, the channels of tree 2 both demonstrated a single change from all liquid to all vapor and back at t = 2.4 s.

Qualitative analysis of the t = 28 min movie showed the visible k = 4 level channels of tree 1 to have void fractions of approximately 0.5. In addition, tree 1 had a slug residing in a k = 3 level channel. Although there was a slug of vapor located in the k = 3 level of tree 1, the location of vapor in the k = 4 level regions provided several clear paths to the test device exit. Multiple exits from tree 1 allowed liquid flow to leave the device, decreasing residence time and the overall amount of boiling. This is unlike tree 2 where bubble growth at both the downstream and upstream bifurcations of the k3cr channel blocked liquid flow, increased vapor residence time, and hence increased boiling.

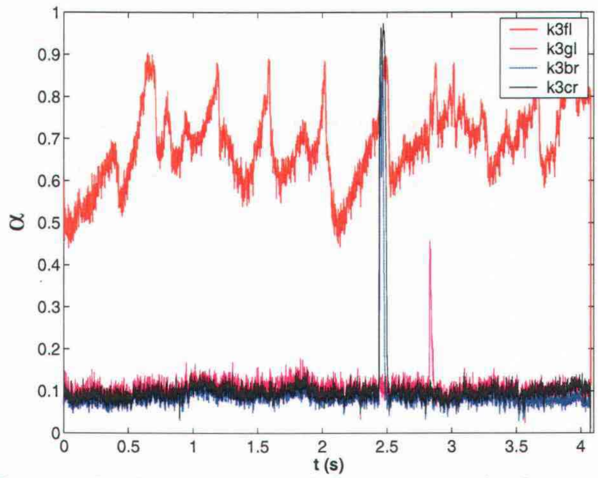

FIGURE 6.17. Regional, time series void fraction in the k = 3 level of trees 1 and 2 associated with t = 28 min movie.

The base-case results were evaluated from several different perspectives. The regional, time-averaged results showed some movies to have larger void fractions than others, especially on the k = 3 level. Streamwise heating may be responsible for larger void fractions in the k = 3 level versus the k = 2 level. The instantaneous data showed these larger, k = 3 level, time-averaged void fractions to be associated with bubble growth (not observed on the k = 2 level), more frequent flashes of vapor, and/or bubbles residing in the channel for the movie duration. Channels on the k = 3 level sometimes demonstrated different behavior despite being subjected to the same conditions. A constant heat flux was applied to the flow, but variable channel dimensions and varying channel surface roughness may have affected the production and residence time of bubbles. Evaluation of the movies indicated channels on a given level were not all the same width. In addition, after the experiments were completed, several channels appeared to experience significant dye residue build-up which could indicate these channels were rougher there or their surface characteristics were affected by dye deposits.

Interaction between branching levels was observed when time series data were evaluated. Vapor in the k = 4 level affected the k = 3 level flow, and the k = 4 and k = 3 levels affected void fraction variation in the k = 2 level. During periods of lower void fraction activity, channels with a shared upstream bifurcation also interacted.

The hydrodynamic behavior of the two trees was similar, but independent. Tree 2 was more active than tree 1. Qualitative observations indicated tree 2 had more active nucleation sites than tree 1.

6.2.2. Case 1 Regional Quantitative Results

The base case results are first compared to those of case 1. Case 1 has the same inlet mass flow rate, 45 g/min, and inlet temperature, 88°C, but the power input was decreased to 61 W. Global measurements of energy input, inlet pressure, temperature, and mass flow rate were sampled at 1000 samples per second. As with the base case, every seven seconds the mean of the 1000 data samples was calculated and recorded. A summary of the case 1 global data from the evaluation period is shown in Fig. 6.18. The average energy input was calculated to be 60.6 W with a standard deviation of the average value equal to 0.24 W. The average inlet pressure was calculated to be 0.74 psig with a standard deviation of 0.021 psig and a standard deviation of the mean equal to 0.001 psig. This inlet pressure is 86% of the inlet pressure associated with the base case. The average inlet mass flow rate was determined to be 44.9 g/min with a standard deviation of the average value calculated to be 0.003 g/min. The average inlet temperature was calculated to be 87.8°C with a standard deviation of 0.003°C and a standard deviation of the mean equal to 0.0002°C.

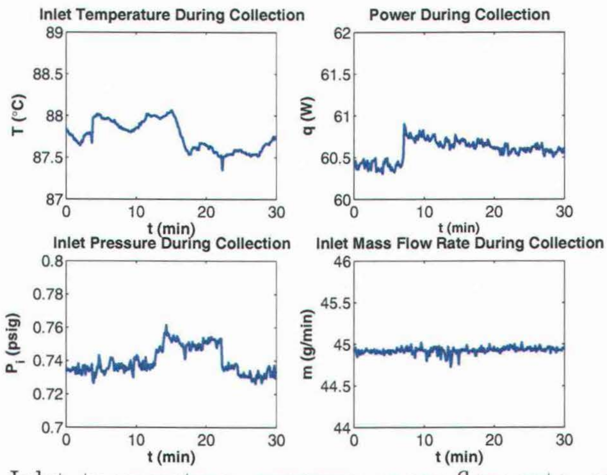

FIGURE 6.18. Inlet temperature, pressure, mass flow rate, and power input measurements of case 1, sampled at 1000 Hz the mean of which was recorded every seven seconds.

Case 1 data will be presented in a manner similar to the base case results, with time-averaged void fraction data followed by instantaneous results. One difference exists, the base-case results pointed to an interaction between the k =2 and k = 3 levels, therefore from this point on these two levels will be evaluated simultaneously.

The regional, time-averaged void fractions calculated for case 1 are compared to those of the base case. The k = 2 level of tree 2 is evaluated first, shown in Fig. 6.19. The base-case, time-averaged void fraction was relatively constant over the course of the experiment. In case 1, the time-averaged void fraction was constant for the first 5 data points, with a slightly larger magnitude than the base case. During the second half of the case 1 experiment, the time-averaged void fraction was variable. In both cases, around t = 15 min the time-averaged void fraction was at a maximum. In the base case it was originally proposed that a change in inlet mass flow rate caused this high point, this was later unsupported when it was shown that tree 1 did not have a similar jump in void fraction at t = 14 min. The global data of case 1 shows no changes occur before, or at, t = 15 min that could explain the large time-averaged void fractions recorded at that time.

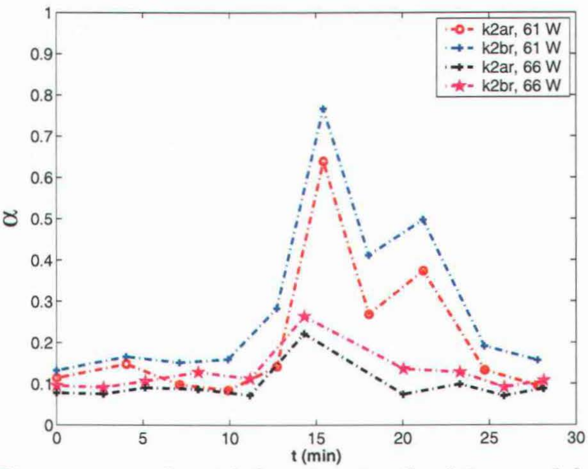

FIGURE 6.19. Time-averaged void fraction in the k2ar and k2br regions was determined for each of the ten movies associated with the base case and case 1.

The time-averaged, k = 3 level void fraction data of case 1 and the base case are compared in Fig. 6.20. Neither case demonstrated consistenly larger void fraction magnitudes. Changes in base-case void fraction from movie to movie were in general smaller than those of case 1. The smaller energy input of case 1 may not provide enough energy to maintain consistent boiling, producing more variable time-averaged void fractions.

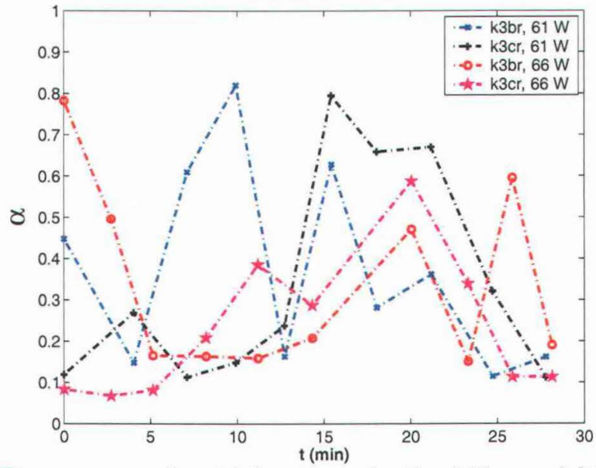

FIGURE 6.20. Time-averaged void fractions in the k3br and k3cr regions were determined for each of the ten movies associated with the base case and case 1.

The case 1 and base-case instantaneous data associated with t = 15.5 min and t = 14 min, respectively, may help explain the large time-averaged void fraction observed in both the k = 2 and k = 3 levels at these times. The time series data from both cases are shown in Fig. 6.21. The k3cr region is located downstream of the k2br region, as was shown in Fig. 6.1. In both the k = 2 and k = 3 levels of case 1, large void fraction changes were 30% more frequent than in the base case. In addition, the flow was all vapor, i.e. void fraction greater than 0.9, for longer periods of time than it is liquid in case 1. On the k = 2 level, as shown in Fig. 6.21(a), the longest all vapor period for the base case, t = 1.6 s to t = 2.2 s, is 40% shorter than the longest all vapor period of case 1, t = 2.7 s to t = 3.7 s. The case 1 data did not show any of the bubble growth observed in the base case

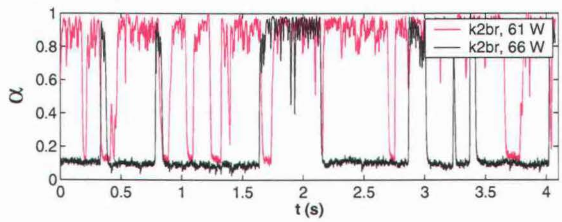

(a)

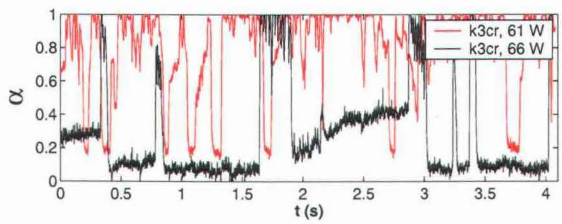

(b)

FIGURE 6.21. Comparison of the instantaneous void fraction in tree 2 during the base case t = 15.5 min movie and case 1 t = 14 min movie. (a) k = 2 level (b) k = 3 level

$k = 3$ level. Two bubble growth periods are observed in the $k = 3$ level of the base case, the first from $t = 0$ s to $t = 0.3$ s and the second at $t = 1.9$ s to $t = 2.8$ s, as seen in Fig. 6.21(b).

Qualitative analysis of the case 1, $t = 15.5$ min movie, showed a void fraction of zero in the $k = 4$ level of tree 2. A small nucleation site near the k3cr upstream bifurcation was observed. Bubbles grew at this location, blocked liquid flow to the k3cr region, and increased flow residence time and vapor production in the $k = 3$ and $k = 2$ levels associated with this bifurcation. The vapor remained in the channels for a longer time period than in the base case, potentially warming the test device which would explain why the flow was more often vapor in case 1 than in the base case. As was true for the base case, vapor in downstream levels affected upstream levels by increasing flow residence time and promoting boiling.

A closer look at the case 1 void fraction in the k3cr region during the time period from $t = 1.325$ s to $t = 1.675$ s, shows none of the rapid oscillations seen in the $k = 3$ level of the base case, shown in Fig. 6.22. A PSD analysis verified that unlike the base case, there are no periodic components associated with this signal.

The case 1 $t = 15.5$ min movie had a large $k = 2$ level time-averaged void fraction. Comparing this movie to one from the base case which also had a significant $k = 2$ level time-averaged void fraction, $t = 14$ min, showed case 1 to experience more frequent changes in void fraction and to be vapor more often than liquid. A nucleation site located in the upstream bifurcation of the k3cr region may be responsible for these results.

A situation where the time-averaged void fraction for both cases was large in the $k = 2$ level is a good place to begin the analysis, but it is necessary to review a few more cases. The instantaneous data associated with movies that have small

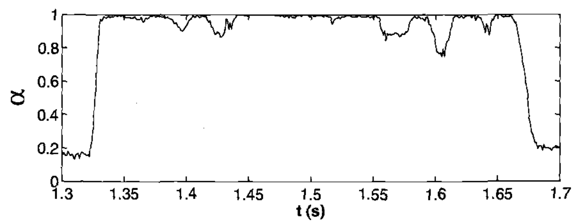

(a)

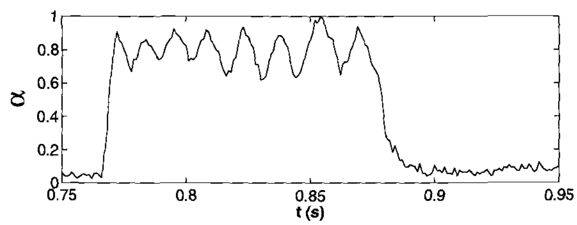

(b)

FIGURE 6.22. Close-up of the instantaneous void fraction in tree 2 during the t = 15.5 min movie of case 1 and the t = 14 min movie of the base case. (a) Case 1 (b) Base Case

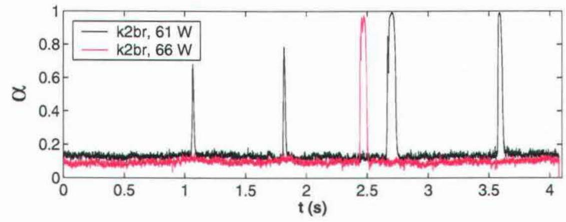

(a)

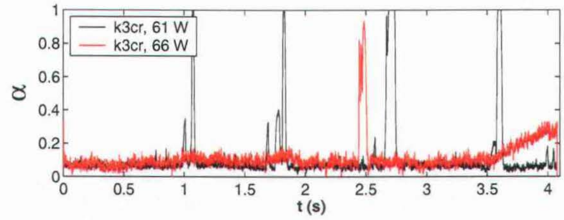

(b)

FIGURE 6.23. Comparison of the instantaneous void fraction in tree 2 during the base case, t = 28 min movie and case 1, t = 28 min movie. (a) k = 2 level (b) k = 3 level

time-averaged void fractions on the k = 2 and k = 3 levels are also evaluated. In addition, when both cases report a time-averaged void fraction of 0.5 in the k = 3 level the time series data are investigated.

Time-averaged void fractions of less than 0.2 were observed in both the k = 2 and k = 3 levels of both cases at t = 28 min. The time series data of the case 1 movie are compared to that of the base case movie in Fig. 6.23. Case 1 experienced several quick flashes of vapor in both levels over the four second period. The base case k = 2 and k = 3 levels experienced only one such change. The base case also demonstrated bubble growth, an increase in void fraction from 0 to 0.3, beginning at t = 3.5 s in the k = 3 level.

Qualitative analysis of the t = 28 min movie of case 1 showed the visible channels of the k = 4 level to be 60% vapor prior to any large change in void fraction. The k3cr region was blocked by a bubble located at its downstream bifurcation and a nucleation site was located at its upstream bifurcation. The nucleation site produced bubbles that blocked flow through the upstream bifurcation. The large amount of vapor in the k = 4 level downstream of k3cr and in k3cr itself slowed the liquid flow and allowed liquid in k3cr and k2br to vaporize. The base case t = 28 min movie demonstrated vapor quantities and locations similar to those seen in case 1. The primary difference between the two cases in this comparison was bubble growth observed in the k = 3 level of the base case. The larger energy input of the base case would be expected to promote more bubble growth.

The instantaneous void fraction variations associated with the t = 0 min movie for case 1 and t = 20 min movie of the base case are shown in Fig. 6.24. These two movies were chosen so a situation not yet evaluated, one with time-averaged void fractions of 0.5 in the k = 3 level, could be investigated. Case 1 experienced bubble growth, void fraction increasing from 0.6 to 1.0, during the period between t = 0 s and t = 1.75 s. The base case also demonstrated periods of bubble growth. Between t = 0 s and t = 1.25 s, t = 1.25 s and 2.25 s, and t = 2.5 s and 3.4 s the void fraction increased from 0.4 to 1.

Reviewing the movie from t = 0 min of case 1, it was seen that a bubble resided in the k3br region during this time period with the k = 4 level channels downstream of it full of vapor. The bubble in the k3br channel slowed liquid flow in this region and in the k = 2 region upstream of it, which promoted boiling in these regions. The k3cr channel and its associated downstream channels contained little to no vapor, allowing liquid flow a path through which it could exit the test

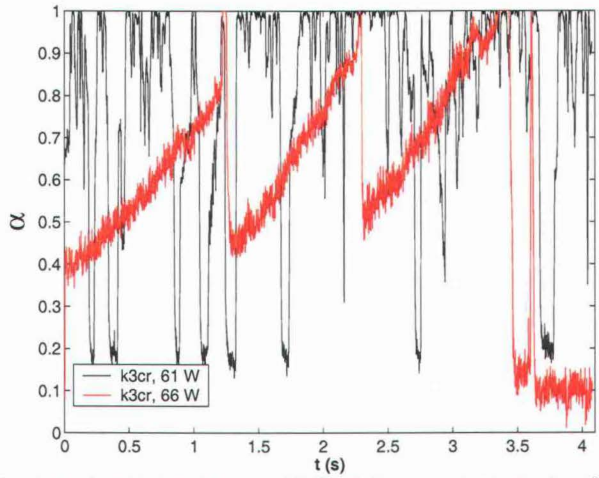

FIGURE 6.24. Regional, time series void fraction variations in the k = 3 level of tree 2 associated with t = 0 min movie of the case 1 and t = 20 min movie of the base case.

device. Liquid flow carrying vapor out of the test device could produce the rapid flashes of vapor observed. With its larger energy input, the base case experienced more bubble growth and less liquid flow, which is most likely the reason why rapid changes in void were not observed for this case.

The objective of this section was to evaluate the void fraction data from case 1; q = 61 W, $\dot{m}$ = 45 g/min, and T_i = 88°; and to compare case 1 results to the base case. Bubble growth in the k = 4 and k = 3 levels during the base case helped promote boiling in the k = 3 and k = 2 levels. The location of the bubbles, blocking some channels, but not others, greatly influenced the amount of vapor generated and the direction it traveled. Case 1 exhibited similar behavior. Less bubble growth in the k = 4 and k = 3 levels was observed and this was believed to affect overall boiling conditions, especially in k = 2 level. A nucleation site located in the upstream bifurcation of the k3cr region produced much of the vapor associated with the k = 3 level void fractions of case 1. In the base case, bubbles were generated in a variety of locations in the k = 3 level rather than in one particular spot, an occurrence attributed to the larger base case power input.

The base case tests were performed before case 1. The nucleation site noted at the k3cr upstream bifurcation in case 1 was not as active in the base case. It is possible that dye sediment from the base case experiment adhered to a rough spot at this location, generating a more active nucleation site. Bubbles generated at this site were largely responsible for the difference in behavior between the two cases. It was expected that the base case would consistently have a larger void fraction, but it did not. The activity at this nucleation site may have produced this difference.

6.2.3. Case 2 Regional Quantitative Results

The base case is now compared to case 2. Case 2 has the same power, 66 W, and inlet temperature, 88°C, as the base case, but for case 2, the mass flow rate was increased to 50 g/min, an 11% increase. Global measurements of energy input, inlet pressure, temperature, and mass flow rate were recorded were sampled at 1000 samples per second. The mean of the 1000 samples was calculated and recorded every seven seconds. A summary of the case 2 global data collected during the evaluation period is shown in Fig. 6.25. The average energy input was calculated to be 66.0 W with a standard deviation of the average value equal to 0.005 W. The average inlet pressure was calculated to be 0.83 psig with a standard deviation of 0.021 psig and a standard deviation of the mean equal to 0.001 psig. This inlet pressure is within 3% of the inlet pressure associated with the base case. At approximately t = 8 min, the pressure dropped 6% below the average, just slightly outside of the uncertainty of this measurement. The average inlet mass flow rate was determined to be 49.5 g/min with a standard deviation of the average value calculated to be 0.003 g/min. The average inlet temperature was calculated to be 87.6°C with a standard deviation of 0.004°C and a standard deviation of the mean equal to 0.0003°C. As was discussed in previous cases, the small but noticeable changes in the mean values are due to manual changes made to the operating conditions.

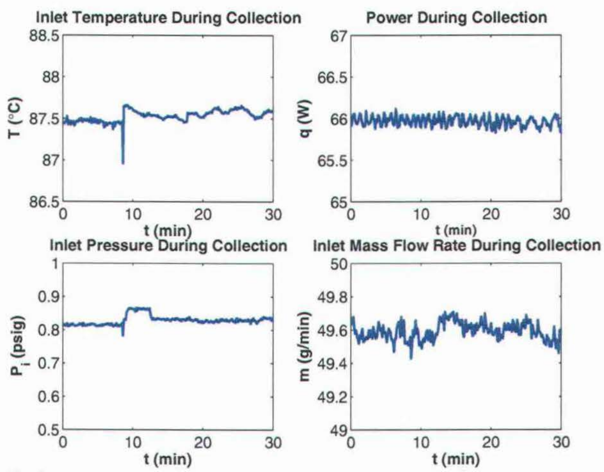

FIGURE 6.25. Inlet temperature, pressure, mass flow rate, and power input measurements of case 2 sampled at 1000 Hz and the mean of the 1000 samples recorded every seven seconds.

Case 2 results are presented in the same order as was used for case 1. The time-averaged regional data of the k = 2 and k = 3 levels of tree 2 are evaluated at the same time. The instantaneous data associated with exceptionally large or small time-averaged void fractions is then examined.

The case 2 time-averaged void fractions in the k = 2 level of tree 2 are compared to those of the base case in Fig. 6.26. The average magnitude of the time-averaged void fraction of the base case is larger than that of case 2. In both cases the time-averaged void fraction is less than 0.1 for 90% of the thirty minute period. In both cases changes in void fraction from movie to movie are small. In case 2, the mass flow rate is 5 g/min faster than the inlet mass flow rate of the base case. A faster mass flow rate, but the same power input, most likely is the reason for the lower time-averaged void fractions observed for case 2 because there is less energy available for latent energy exchange.

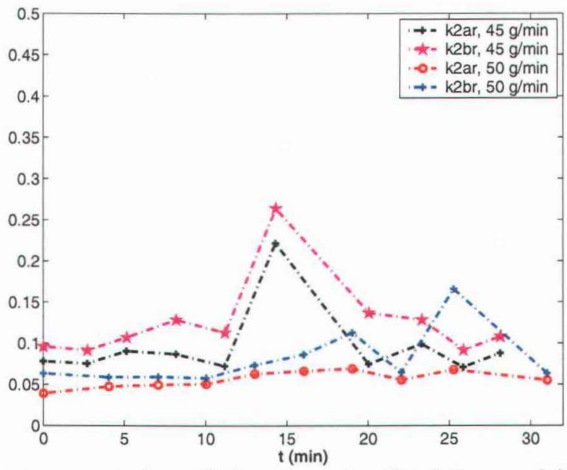

FIGURE 6.26. Time-averaged void fractions in the k2ar and k2br regions determined for each of the ten movies associated with the base case and with case 2.

When comparing the time-averaged void fractions of case 2, in the k = 3 level of tree 2, with those of the base case, several observations can be made. Figure 6.27 shows the time-averaged void fractions of the base case were larger than those of case 1 80% of the time. Case 2 void fractions were more variable. In case 2, void fraction changes from movie to movie in the k3br and k3cr regions were different. In the base case it was observed that channels on the k = 3 level that do not share an upstream bifurcation often demonstrate similar void fraction variations. The faster mass flow rate may be responsible for differences between case 2 k = 3 level channel activity and that of the base case. The power supplied, 66 W, may not be sufficient to maintain consistent boiling at this accelerated flow rate.

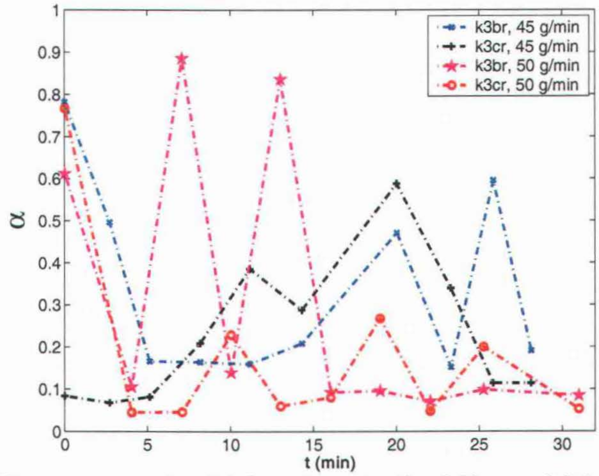

FIGURE 6.27. Time-averaged void fractions in the k3br and k3cr regions determined for each of the ten movies associated with the base case and case 2.

As was true for the base case and case 1, the time series data associated with exceptional points on the time-averaged void fraction plots are evaluated. Small, less than 0.2, time-averaged void fractions in the k = 2 level occurred at t = 28 min for the base case and t = 31 min for case 2. The instantaneous data of these two cases are compared in Fig. 6.28. On the k = 2 level, case 2 had a constant void fraction, less than 0.1, for the entire movie. Examining all ten movies taken during the case 2 study, only 50% of the movies experienced void fraction changes in the k = 2 level. The average number of void fraction changes in those movies was one. Significant bubble growth in other levels witnessed during qualitative analysis ensures the flow was in fact boiling.

For the movie recorded at t = 31 min, the k = 3 level had no significant changes in void. This was the only movie of the ten associated with case 2 that did not have activity. The t = 31 min movie represents an anomaly.

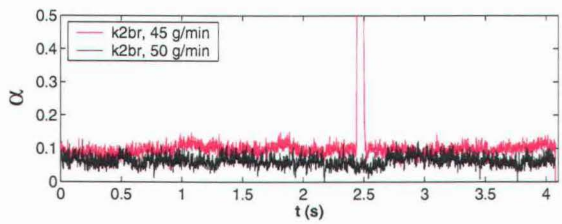

(a)

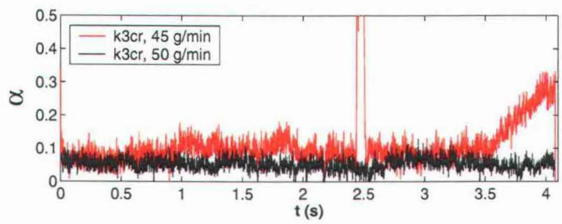

(b)

FIGURE 6.28. Comparison of the instantaneous void fraction variations in tree 2 during the base case, t = 28 min movie, and the case 1, t = 31 min movie. (a) k = 2 level (b) k = 3 level

Qualitative analysis of the t = 31 min movie of case 2 showed the k = 4 level channels of tree 2 to be 40% vapor. These bubbles grew and coalesced during the four second movie, but do not grow large enough to enter the upstream channel, as was often seen in the base case. Each k = 3 level channel had at least one k = 4 channel directly downstream completely free of vapor. Therefore, liquid flow had clear paths through which it could exit the test device. The slowing of liquid flow and the subsequent promotion of boiling noted in the base case may have been prevented by the unblocked exit paths available during this case 2 movie.

The largest case 2 time-averaged void fraction of the k = 2 level of tree 2 occurred at t = 25 min. The t = 14 min movie of the base case, represented the largest tree 2, k = 2 level time-averaged void fraction for that study. The instantaneous data associated with both movies are compared in Fig. 6.29. In case 2, there was one change from all liquid to all vapor and back in the k = 2 and k = 3 levels. In addition, case 2 demonstrated bubble growth in the k3cr region. The void fraction increased from 0 to 0.2 and 0 to 0.4 twice, between t = 2.25 s and t = 2.75 s and then again between t = 3.0 s and t = 4 s. The base case experienced several large, rapid changes in void fraction in both the k = 2 and k = 3 levels. In addition the k3cr channel demonstrated a period of bubble growth during the base case, the void fraction increased from 0.1 to 0.5, between t = 1.9 s and t = 2.8 s. Observations show the two movies to have similar vapor quantities and locations, including bubble production at the upstream bifurcation of the k3cr region. The faster flow rate of case 2 may result in slightly less bubble production at this site.

Similar to the base case, case 2 demonstrated definite interaction between the k = 2 and k = 3 levels. Looking for further similarities, the case 2 void fraction in the k2br region, between t = 2.65 s and t = 3 s is compared to the base case

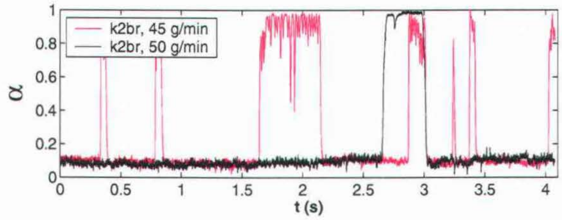

(a)

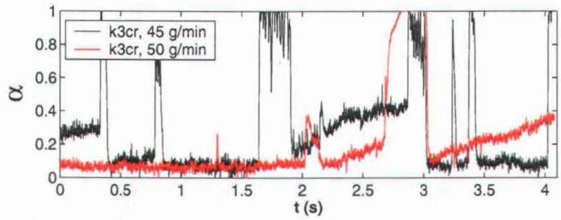

(b)

FIGURE 6.29. Comparison of the instantaneous void fraction in tree 2 during the base case, t = 14 min movie, and the case 1, t = 25 min movie. (a) k = 2 level (b) k = 3 level

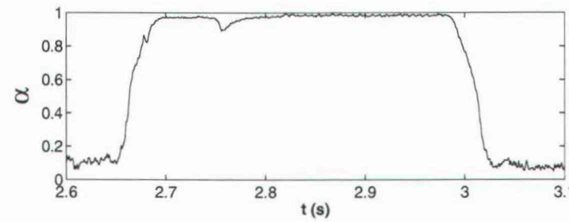

(a)

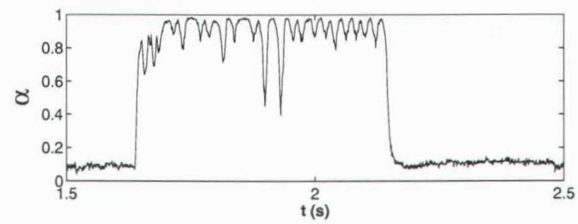

(b)

FIGURE 6.30. Close-up of the instantaneous void fraction in tree 2 during the base case t = 14 min movie and case 1 t = 25 min movie. (a) Case 2 (b) Base Case

in Fig. 6.30(a). The case 2 void fraction was greater than 0.9 and appeared to experience high frequency oscillations during this time period. Looking at a portion of the base case movie when the average void fraction was large, shown in Fig. 6.30(b), the void fraction oscillated, but at a much lower frequency. A PSD analysis of the case 2 void fraction during this time period indicates it oscillated at 150 Hz compared to 50 Hz for the base case oscillations.

The final data sets to be evaluated are those that represent the large k = 3 level time-averaged void fractions in both case 2 and the base case. These data sets are compared in Fig. 6.31. Case 2 was all liquid for the first half of the t = 10 min movie. During the second half of the four second time period a small bubble grew to fill 50% of the region. The base case experienced three periods of bubble growth, the void fraction increased from 0.3 to 1.0, during the t = 12 min movie.

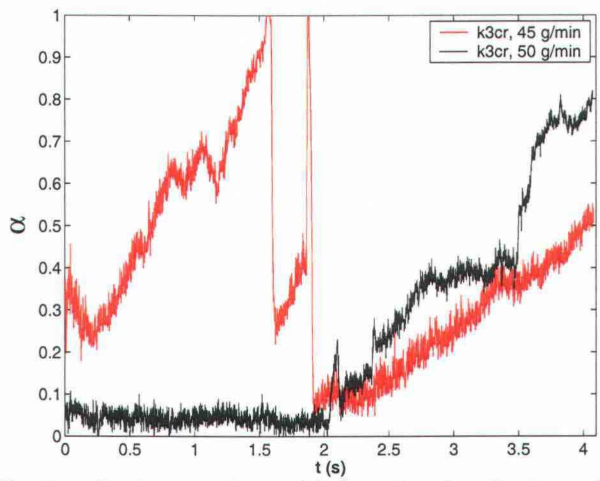

FIGURE 6.31. Regional, time series void fraction in the k = 3 level of tree 2 associated with t = 12 min movie of the base case and t = 10 min movie of case 2.

A qualitative analysis of the case 2, t= 10 min movie showed 60% of the k = 4 level channels of tree 2 were full of vapor during the first two seconds of the movie. In addition, bubbles blocked the upstream bifurcations of k3br and k3cr. The large vapor volume in tree 2 increased liquid flow residence time and increased vaporization in the k = 3 level. In the base case, similar vapor quantities and locations resulted in more frequent void fraction variations. Most likely, the faster flow rate prevented enough energy from being added to the liquid flow to maintain the same level of phase change seen in the base case. The surface tension force associated with the bubble in the k3cr channel during the t = 10 min movie was compared to the associated momentum force, both forces were calculated in the manner described in Section 6.2.1. The surface tension was an order of magnitude larger than the inertia force despite the increased mass flow rate. In fact, the vapor velocity in this region was slower during this case 2 movie than the vapor velocity determined for a similar situation in the base case study.

Comparing case 2 to the base case, the overall amount of vapor and void fraction variations are smaller for case 2. The faster flow rate may decrease the amount of time energy can be added to the flow, which would lower the average flow temperature and decrease the amount of phase change.

6.2.4. Base-Case Local Quantitative Results

It was observed during regional analysis that branching levels interact. Branching levels are specific to the fractal-like design, therefore this geometry affects void fraction variations. A localized study at the bifurcations will further investigate the effects of the fractal-like geometry on two-phase flow.

Four bifurcations were examined, they are shown outlined in blue in Fig. 6.32. Each of the four bifurcations is divided into three parts; an entrance, right exit, and left exit; all of which are labeled.

Similar to the regional study, the base case local results will be evaluated and compared to those of case 1 and 2. Time-averaged data points will be investigated first followed by an analysis of instantaneous data.

The local, time-averaged void fraction data of the bifurcation located downstream of the k2br channel is shown in Fig. 6.33. This bifurcation is the primary focus of this study due to observations made during the qualitative analysis. Data at each bifurcation was taken simultaneously and the average calculated in the same manner as was described in Section 6.2. The local, time-averaged void fractions experienced small changes, never increasing more than 0.2, from movie

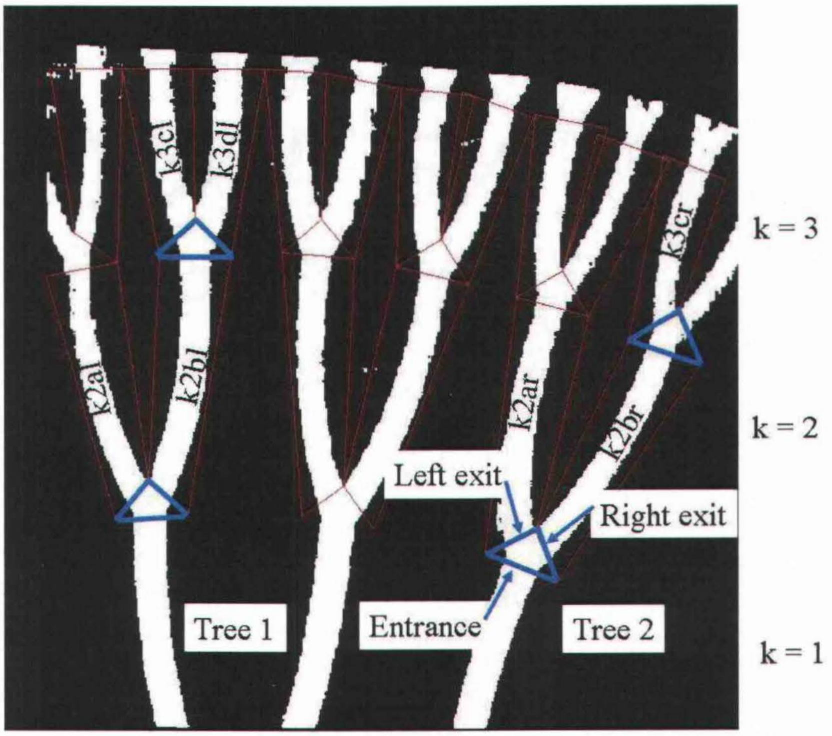

FIGURE 6.32. Bifurcations outlined in blue were the focus of the local study.

to movie, as seen in Fig. 6.33. The bifurcation exits displayed symmetric void fraction variations, but the magnitudes were different.

Qualitative analysis indicated that there often was upstream movement of vapor. Vapor moving upstream in a channel would reach the upstream bifurcation of that channel, hook around the apex of the bifurcation, and begin moving downstream through the channel that shares the bifurcation. For example, vapor moving upstream in the k2br channel entered the right exit of the bifurcation shared by the k2ar and k2br regions, hooked around the bifurcation, and began moving downstream in k2ar channel. This frequently observed flow pattern may explain why the right exit consistently had a larger void fraction than the left exit and entrance of this bifurcation.

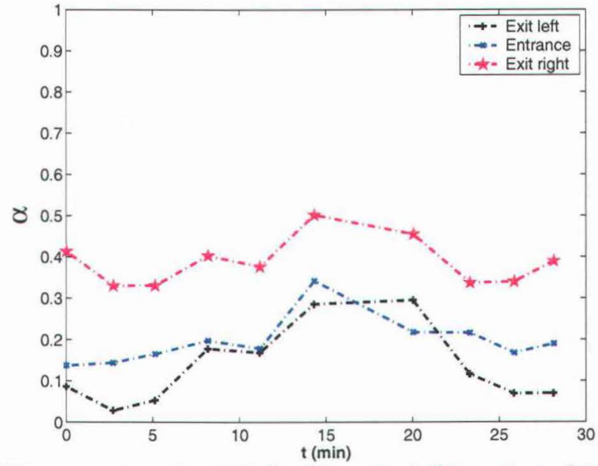

FIGURE 6.33. Time-averaged void fraction in bifurcation downstream of the k2br channel during the base case.

At t = 3 min, the local time-averaged void fraction was small, less than 0.2 in the left exit and entrance and about 0.3 in the right exit, as shown in Fig. 6.33. The time series data of this movie, seen in Fig. 6.34(a), shows the void fraction changed frequently during the four second movie. Several large changes in void fraction occur between t = 3 s and t = 4 s. The magnitude of the right exit void fraction was consistently larger than that of the left exit. Figure 6.34(b) shows that right exit void fraction variations that occurred during the time period from t = 3.65 s to t = 3.75 s, also happened in the left exit after a small time delay.

Bubble development just downstream of the right exit was observed during qualitative analysis. A bubble resided at this location for most of the movie oscillating and causing the larger right exit void fraction. Eventually the bubble grew upstream, hooked around the bifurcation, and moved downstream after it passed through the left exit.

The t = 3 min movie was evaluated for its rather small, local, time-averaged void fraction. The movie from t = 14 min represents the other end of the spectrum,

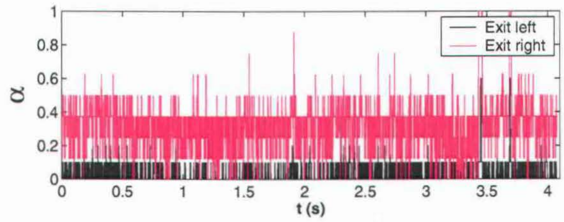

(a)

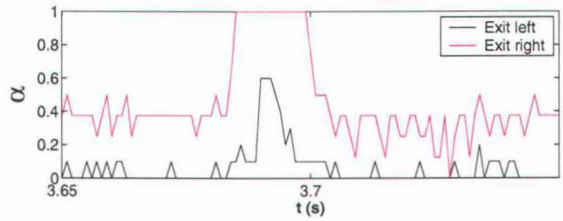

(b)

FIGURE 6.34. Variations in local void fraction during t = 3 min at the bifurcation located downstream of the k2br channel. (a) Full movie (b) t = 3.65 s to t = 3.75 s

with large local, time-averaged void fractions, as seen in Fig. 6.33. The average values of these void fractions all exceed 0.25. The time series data of this movie is evaluated next.

The instantaneous data from the t = 14 min movie, seen in Fig. 6.35(a), shows many significant void fraction changes at the right exit. These data appear to be discretized, this is due to number of pixels contained within the line of interest not being large enough. As was true for the t = 3 min case, the right exit void fraction was consistently larger than that of the left exit. Changes observed at the right exit also occurred at the left exit after a small time delay, seen in Fig. 6.35(b). This behavior was similar to that seen in the t = 3 min movie, but with a larger magnitude and frequency. Qualitative analysis indicated the

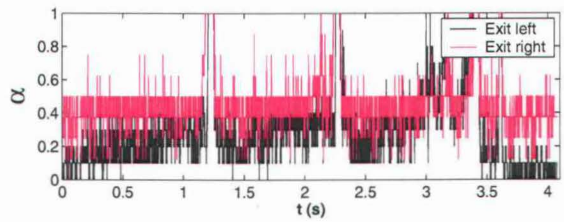

(a)

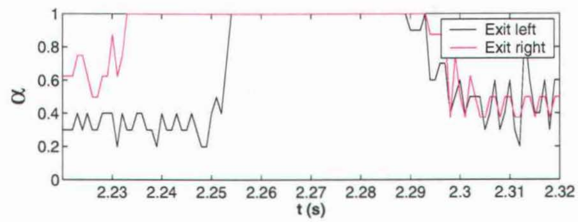

(b)

FIGURE 6.35. Variations in local void fraction during t = 14 min at the bifurcation located downstream of the k2br channel. (a) Full movie (b) t = 2.21 s to t = 2.32 s

same bubble development noted at the downstream side of the right exit of the bifurcation in the t = 3 min movie also occurred for the t = 14 min movie.

In the two cases just evaluated, the vapor moved upstream in the k = 3 level and entered the right exit of the bifurcation rather than the entrance. A movie in which the vapor entered the bifurcation through the entrance is now evaluated to see if different behavior is observed.

During the t = 28 min movie vapor entered the bifurcation downstream of the k2bl channel of tree 1 through the entrance. Time series data for this movie, plotted in Fig. 6.36(a), showed two significant changes in void occurred during the four second interval. The first change was seen at t = 2.8 s and the second at t = 3 s. A closer look at these changes showed the bifurcation entrance void

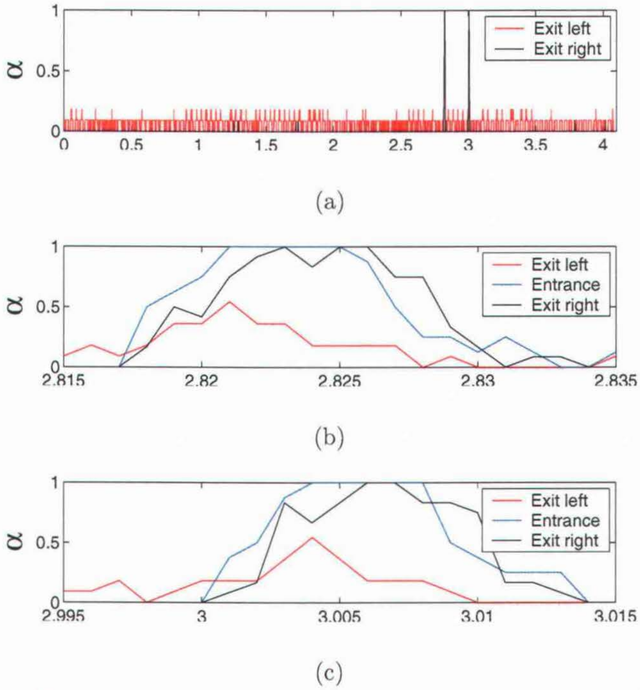

FIGURE 6.36. Variations in local void fraction during t = 28 min at the bifurcation located downstream of the k2bl channel. (a) Full movie (b) t = 2.815 s to t = 2.835 s (c) t = 2.995 s to t = 3.105 s

fraction increased to 1 before either of the exits. The left exit reached its maximum void, 0.5, just after the entrance. Then the right exit filled with vapor. Evaluation of the t = 28 min movie showed that significant bubble growth occurred in the region downstream of the left exit. This growth may increase resistance to liquid and vapor flow in the channel downstream of the left exit and force a right exit preference.

Instantaneous data associated with another movie, taken at t = 26 min, where the vapor originates upstream of the bifurcation is shown in Fig. 6.37(a). A single large change in void fraction occurred at the bifurcation upstream of the

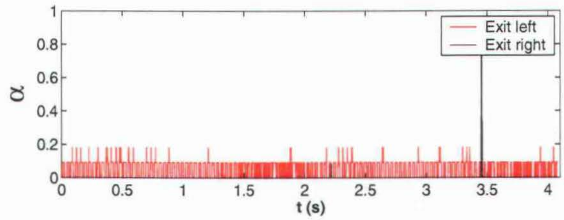

(a)

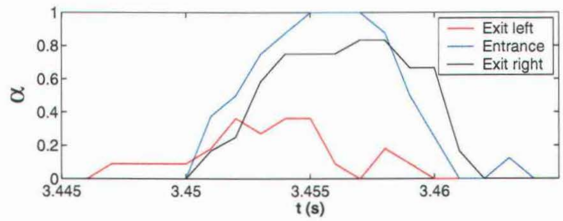

(b)

FIGURE 6.37. Variations in local void fraction during t = 26 min at the bifurcation located downstream of the k2bl channel. (a) Full movie (b) Close-up

k2bl channel of tree 1, as shown in Fig. 6.32, at t = 3.45 s. A close-up of the time period between 3.445 s to 3.465 s is shown in Fig. 6.37(b). During this time, the entrance filled with vapor, and the right exit reached its maximum void fraction, 0.8, 0.0025 seconds later. There was vapor in the left exit prior to the filling of the entrance. Watching the movie from t = 26 min, bubble growth above the left exit was observed. This bubble growth would be responsible for the increase in void fraction in the left exit prior to any vapor entering the bifurcation entrance. In addition, the location of this bubble, above the left exit, could be responsible for preference, larger void fraction, in the right exit.

In summary, two movies from the base case in which vapor entered the bifurcation through one exit and left through the other were investigated. The bifurcation converted upstream vapor flow through one channel to downstream flow in the channel with which it shares an upstream bifurcation. Two additional cases were evaluated where the vapor entered the bifurcation through the entrance and left through the exits. In this situation the bifurcation split the void between the two downstream channels. There appears to be a preference for the right exit, but it was observed that there was always some pre-existing vapor volume downstream of the left exit, which could be causing this predilection.

6.2.5. Case 1 Local Quantitative Results

The case 1 local time-averaged data are compared to the base-case, local, time-averaged data in Fig. 6.38. Again, case 1 has a power level of 61 W, while the base-case power was 66 W. Case 1 local time-averaged void fractions experience smaller changes from movie to movie than the base case. In the base case, the right exit consistently experienced the largest void fraction; in case 1 neither exit void fraction had a consistently larger magnitude. It was proposed that vapor located downstream of the left exit could be responsible for the right exit preference in the base case, the time series data associated with case 1 will be investigated to see if similar reasoning can be applied to the lack of exit preference seen in this case.

The case 1 movie from t = 4 min was one of the very few in which vapor moved downstream through the bifurcation. The time series data shows the left exit maintained an average void of 0.7 for the majority of the movie, as seen in Fig. 6.39(a). A close-up of the void fraction variations between 1.97 and 2.02 s, is shown in Fig. 6.39(b). Vapor entered the entrance first, but the entrance did not reach a void fraction of 1 before either of the exits. Bubbles resided just above the right and left exits during this movie moving upstream and filling the exit

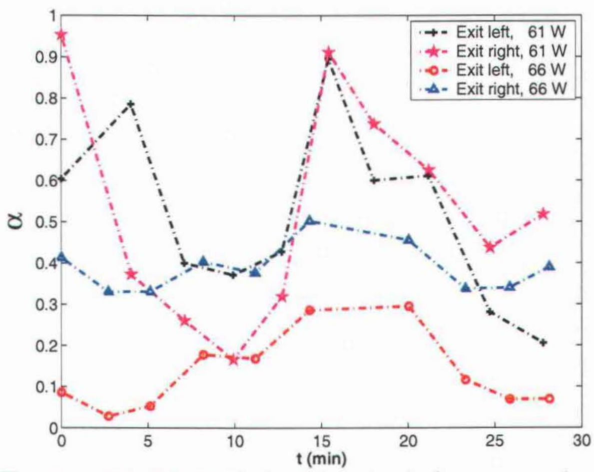

FIGURE 6.38. Time-averaged void fraction in bifurcation downstream of the k2br channel during case 1.

with vapor. It appears that this downstream vapor allowed the void fraction in the exits to increase to one before that of the entrance. No other movies with a downstream moving void were recorded for case 1.

6.2.6. Case 2 Local Quantitative Results

The case 2 local time-averaged data associated with the bifurcation downstream of the k2br channel is compared to the base-case local time-averaged data of the same location in Fig. 6.40. The case 2 mass flow rate, 50 g/min, was 5 g/min faster than the base case flow rate. All other parameters were the same. The case 2, local, time-averaged void fractions associated with the left exit of the bifurcation experienced small changes from movie to movie. The right exit demonstrated large void fraction variations during the first fifteen minutes of the evaluation period. Unlike the base case, case 2 did not demonstrate symmetric

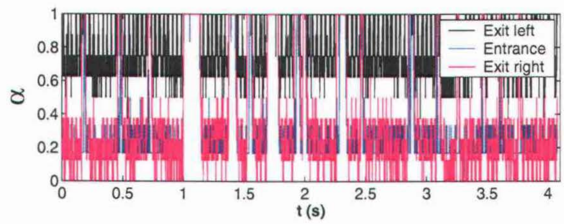

(a)

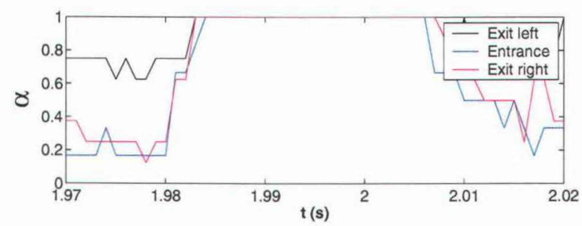

(b)

FIGURE 6.39. Variations in local void fraction during t = 4 min movie of case 1 at the bifurcation located downstream of the k2br channel. (a) Full movie (b) Close-up

void fraction changes between the right and left exits. Like the base case, case 2 showed a vapor flow preference for the right exit of the bifurcation.

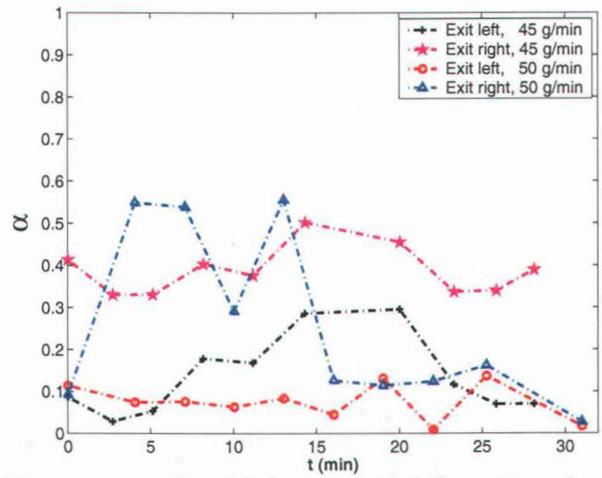

FIGURE 6.40. Time-averaged void fraction in bifurcation downstream of the k2br channel during case 2.

A qualitative analysis of all the case 2 movies showed the t = 18 min movie to have vapor moving towards the entrance of the bifurcation located downstream of the k2br region. The instantaneous void fraction data for this movie is shown in Fig. 6.41(a). During the time period between 2.01 s and 2.06 s, the entrance void fraction reached one just before the two exits. The right exit was filled with vapor milliseconds after the left exit. Evaluation of the t = 18 min movie showed there to be some vapor downstream of the right exit. In the base case, vapor located downstream of an exit typically resulted in a lower void fraction at that exit. The void fraction variations in Fig. 6.41(b) suggest that downstream vapor slowed vapor flow through the right exit but did not affect the quantity of vapor passing through the bifurcation exit.

A local study of void fraction variations at specific locations within the bifurcations of trees 1 and 2 was performed. In all three cases, vapor that origi-

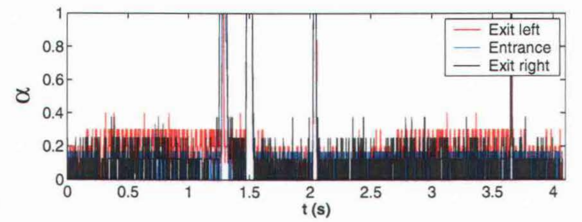

(a)

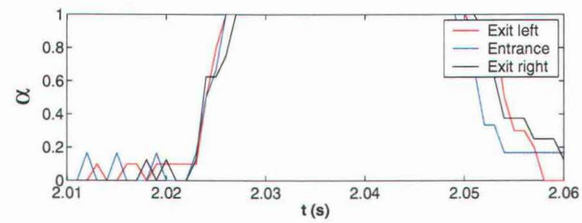

(b)

FIGURE 6.41. Variations in local void fraction during t = 18 min movie of case 2 at the bifurcation located downstream of the k2br channel. (a) Full movie (b) Close-up

nates upstream of the bifurcation, moved through the entrance of the bifurcation, and was divided between the two channels downstream of the bifurcation. The split between downstream regions was not always even, maldistributions occurred. Vapor located downstream of the bifurcation may have affected the quantity of vapor distributed to each channel. In addition, flow that moved upstream through the device was redirected by the bifurcation. This flow pattern is different than that observed in parallel channel devices, where upstream moving flow continues all the way to the device inlet plenum.

7. CONCLUSION

Two-phase flow experiments were performed in a fractal-like branching channel network. Data collected in the form of images were evaluated for local and regional void fraction variations. The results from a single case were evaluated qualitatively. This case, the base case, had a power level of 66 W, an inlet mass flow rate of 45 g/min, and an inlet temperature of 88°. Observations made during qualitative analysis of the base case were used to define a quantitative study of that case. The base-case results were then compared to two other cases. Case 1 had the same inlet mass flow rate and inlet temperature as the base case, but the power input was decreased to 61 W. Case 2 had the same power and inlet temperature as the base case, but the mass flow rate was increased to 50 g/min.

Ten movies from the base case were evaluated from a qualitative standpoint. In the k = 2 level, a combination of single phase and slug flow were observed. In the k = 3 level, single phase, bubbly, and slug flow were noted.

Base-case void fraction variations in each channel, excluding the bifurcation, were analyzed first. These regional, time-averaged void fractions were shown to be larger on the k = 3 level than the k = 2 level. This was most likely due to streamwise heating of the flow. Regional, instantaneous data suggested different branching levels interact. Vapor in the k = 4 level affected the k = 3 level flow, and the k = 4 and k = 3 levels affected void fraction variation in the k = 2 level. It was also observed that channels with a shared upstream bifurcation interact. In addition, a comparison of surface tension forces to inertia forces in the k = 3 level showed the surface tension to be an order of magnitude larger, suggesting this force to play an important role in microscale two-phase flow. The hydrodynamic behavior of two different trees was shown to be similar, but independent. Tree 2 was more active than tree 1. Qualitative observations indicated tree 2 had more active nucleation sites than tree 1.

Two observations were made from a local study that focused on the bifurcations. Vapor flow moving upstream through the device is redirected by a bifurcation and moves downstream through the channel which shared this particular bifurcation. This flow pattern is different than that reported in previous investigations of two-phase flow in parallel channel devices, where upstream moving flow continues all the way to the device inlet plenum. Vapor flow moving downstream through a channel is split by the bifurcation, the quantity distributed to each channel depends on downstream void conditions.

Comparison of base-case results with case 1 and case 2 indicates increasing the flow rate and decreasing the power, respectively, produces void fraction variations that follow the same trends as those witnessed in the base case, but with different magnitudes and frequencies.

This was the first two-phase flow study to be performed in the fractal-like geometry. Several recommendations can be made to improve future studies. First, it is suggested that the test device channel dimensions and surface roughness be quantified prior to any testing. Knowledge of these characteristics would help explain observed behaviors. Due to the apparent impact of vapor in $k = 4$ level branches it is also recommended that a lens configuration capable of imaging these channels at a sufficient resolution be used. In addition, if these experiments could be repeated without fear of breaking the test devices, it would be beneficial to increase the power level beyond 66 W. For the local study, it is suggested that the number of pixels making up a line could be increased. Finally, inlet conditions were measured 6.96 mm from the actual test device inlet. In future works, it is recommended that these measurements be made at the test device inlet.

BIBLIOGRAPHY

[1] Steinke, M.E. and Kandlikar, S.G., "Flow Boiling and Pressure Drop in Parallel Flow Microchannels," Proceedings of the First International Conference on Microchannels and Minichannels, Rochester, N.Y., pp. 567-579, 2003.

[2] Jiang, L. and Wong, M., "Forced Convection Boiling in a Microchannel Heat Sink," *Journal of Microelectromechanical Systems*, vol. 10, pp. 80-87, 2001.

[3] Zhang, L., Koo, J-M., Jiang, L., Asheghi, M., Goodson, K., Santiago, J., and Kenny, T., "Measurements and Modeling of Two-Phase Flow in Microchannels With Nearly Constant Heat Flux Boundary Conditions," *Journal of Microelectromechanical Systems*, vol. 11, no. 1, pp. 12-19, 2002.

[4] Wu, H.Y. and Cheng, P., "Visualization and Measurements of Periodic Boiling in Silicon Microchannels," *International Journal of Heat and Mass Transfer*, vol. 46, pp. 2603-2614, 2003.

[5] Qu, W. and Mudawar, I., "Measurement and Prediction of Pressure Drop in Two-Phase Microchannel Heatsinks," *International Journal of Heat and Mass Transfer*, vol. 46, pp. 2737-2753, 2003.

[6] Tuckerman D.B. and Pease, R.F.W., "High Performance Heat Sinking for VLSI," IEEE Electron Device Letters, ED1-2, pp. 126-277, 1981.

[7] Bau, H.H., "Optimization of Conduits' Shape in Micro Heat Exchangers" *International Journal of Heat and Mass Transfer*, vol. 41, pp. 2717-2723, 1998.

[8] West G.B., Brown, J.H., and Enquist, B.J., "A General Model for the Origin of Allometric Scaling Laws in Biology," *Science*, vol. 276, pp. 122-126, 1997.

[9] Pence, D.V., "Improved Thermal Efficiency and Temperature Uniformity Using Fractal-Like Branching Channel Networks," Proceedings of the International Conference on Heat Transfer and Transport Phenomena in Microscale, Bergell House, New York, pp. 142-148, 2000.

[10] Pence, D.V., "Reduced Pumping Power and Wall Temperature in Microchannel Heat Sinks With Fractal-Like Branching Channel Networks," *Microscale Thermophysical Engineering*, vol. 6, pp. 319-330, 2002.

[11] Alharbi, A.Y., Pence, D.V., and Cullion, R.N., "Fluid Flow Through Microscale Fractal-like Branching Channel Networks," *Journal of Fluids Engineering*, vol. 125, pp. 1051-1057, 2003.

[12] Bejan, A., "Constructal Tree Network for Fluid Flow between a Finite Size Volume and One Source or Sink," *Revue Generale de Thermique*, vol. 36, pp. 592-604, 1997.

[13] Pence, D.V. and Enfield, K.E., "Inherent Benefits in Microscale Fractal-Like Devices for Enhanced Transport," *Design and Nature*, Rhodes, Greece, 2004.

[14] Boure, J.A., Bergles, A.E., and Tong, L.S., "Review of Two-Phase Flow Instability," *Nuclear Engineering and Design*, vol. 25, pp. 165 - 192, 1973.

[15] Saha, P. and Zuber, N., "Point of Net Vapor Generation and Vapor Void Fraction in Subcooled Boiling," Proceedings of the Fifth International Heat Transfer Conference, Tokyo, pp. 175-179, 1974.

[16] Kennedy, J.E., Roach, G.M., Dowling, M.F., Abdel-Khalik, S.I., Ghiaasiaan, S.M., Jeter, S.M., and Quershi, Z.H., "The Onset of Flow Instability in Uniformly Heated Horizontal Microchannels," *Journal of Heat Transfer*, vol. 122, pp. 118-125, 2000. 9.

[17] Warrier, G.R. and Dhir, V.K., "Visualization of Flow Boiling in Narrow Rectangular Channels," *Journal of Heat Transfer*, vol. 126, pg. 495, 2004.

[18] Bowers, M.B. and Mudawar, I., "High Flux Boiling in Low Flow Rate, Low Pressure Drop Mini-Channel and Micro-Channel Heat Sinks," *International Journal of Heat and Mass Transfer*, vol. 37, pp. 321-332, 1993.

[19] Koo, J-M., Jiang, L., Zhang, L., Zhou, P., Banerjee, S., Kenny, T.W., Santiago, J.G., and Goodson, K.E., "Modeling of Two-Phase Microchannel Heat Sinks For VLSI Chips," Proceedings of the IEEE Micro Electro Mechanical Systems, Interlaken, pp. 422 - 426, 2001.

[20] Wilkes, James O., *Fluid Mechanics for Chemical Engineers*, Prentice Hall, New Jersey, 1999.

[21] Tong, L.S. and Tang, Y.S., *Boiling Heat Transfer and Two-Phase Flow*, Second Edition, Taylor Francis, Washington, D.C., 1997.

[22] Triplett, K.A., Ghiaasiaan, S.M., Abdel-Kahlik, S.I., LeMouel, A., McCord, B.N., "Gas-Liquid Two-Phase Flow in Microchannels Part II: Void Fraction and Pressure Drop," *International Journal of Multiphase Flow*, vol. 25, pp. 395-410, 1999.

[23] Chung, P.M.-Y. and Kawaji, M., "The Effect of Channel Diameter on Adiabatic Two-Phase Flow Characteristics in Microchannels," *International Journal of Multiphase Flow*, vol. 30, pp. 735-761, 2004.

[24] Kandlikar, S.G., "Heat Transfer Mechanisms During Flow Boiling in Microchannels," *Journal of Heat Transfer*, vol. 126, pp. 8-16, 2004.

[25] Bergles and Kandlikar, "On the Nature of Critical Heat Flux in Microchannels," *Journal of Heat Transfer*, vol. ENTER, pp. 101-107, 2005.

[26] Figliola, R.S. and Beasley, D.E., *Theory and Design for Mechanical Measurements*, Third Edition, John Wiley and Sons, New York, 2000.

APPENDICES

APPENDIX A. Calibration

The calibration unit used to calibrate both the pressure transducer and RTD was an Omega Calibration Unit, model number PCL-1B, serial number 9955. The pressure module used with the calibration unit was also from Omega, model number PCL-MB, serial number GQS-26484. The pressure module had a range of 0-100 psia and an accuracy of .05% of full scale. The equation associated with the calibration curve is shown in Eq. A.1.

$$y = 34.2x - 11.82 \tag{A.1}$$

The temperature module used with the calibration unit was also from Omega, model number PCL-MR-1, serial number GRT-3605. The temperature module range is 400Ω. The equation associated with the calibration curve is shown in Eq. A.2.

$$y = 2.63x - 262.96 \tag{A.2}$$

The mass flow meter did not require calibration. The output of this device was a 0 to 10 V square wave, a frequency of 1000 Hz was associated with a flow rate of 2 g/min.

$$y = x\frac{2}{1000} \tag{A.3}$$

APPENDIX B. MATLAB Algorithms

B.1. Qualitative Analysis

```
%%%%%%%%%%%%%%%%%%%%%%%%%%%%%%%%%%%%%%%%%%%%%%%%%%%%%%%%%%%%%%%%%%%
%
% qualanalysis.m
% Rebecca Cullion
% 2005
%
%%%%%%%%%%%%%%%%%%%%%%%%%%%%%%%%%%%%%%%%%%%%%%%%%%%%%%%%%%%%%%%%%%%
%
% This m file reads in an image, crops out undesired components,
% adjusts image contrast, and binarizes resultant image.
%
% Input = images to be evaluated.
%
%%%%%%%%%%%%%%%%%%%%%%%%%%%%%%%%%%%%%%%%%%%%%%%%%%%%%%%%%%%%%%%%%%%

% read in images of interest
img1 = imread('img00996.bmp');
img2 = imread('img00997.bmp');
img3 = imread('img00998.bmp');
img4 = imread('img00999.bmp');

% convert images from uint8 to double
imgd1 = double(img1);
imgd2 = double(img2);
imgd3 = double(img3);
imgd4 = double(img4);

% read in previously defined mask and convert to double
mask = imread('mask.bmp');
maskd = double(mask);

% use mask to crop images
imgcrop1 = maskd.*imgd1;
imgcrop2 = maskd.*imgd2;
imgcrop3 = maskd.*imgd3;
imgcrop4 = maskd.*imgd4;

% convert cropped images back to uint8 for further processing
imgcrop1 = uint8(imgcrop1);
imgcrop2 = uint8(imgcrop2);
imgcrop3 = uint8(imgcrop3);
imgcrop4 = uint8(imgcrop4);

% adjust image contrast
imgadj1 = imadjust(imgcrop1,stretchlim(imgcrop1),[0 1]);
imgadj2 = imadjust(imgcrop2,stretchlim(imgcrop2),[0 1]);
imgadj3 = imadjust(imgcrop3,stretchlim(imgcrop3),[0 1]);
imgadj4 = imadjust(imgcrop4,stretchlim(imgcrop4),[0 1]);
```

B.2. Quantitative Analysis

```
%%%%%%%%%%%%%%%%%%%%%%%%%%%%%%%%%%%%%%%%%%%%%%%%%%%%%%%%%%%%%%%%%%%%
% regseqproc.m
% Edited by Rebecca Cullion
% 2005
%%%%%%%%%%%%%%%%%%%%%%%%%%%%%%%%%%%%%%%%%%%%%%%%%%%%%%%%%%%%%%%%%%%%
% This m file reads in the base and data images. It then calls
% several associated m files required for region definition,
% image processing, and pixel counting.
%%%%%%%%%%%%%%%%%%%%%%%%%%%%%%%%%%%%%%%%%%%%%%%%%%%%%%%%%%%%%%%%%%%%
clear all
close all

iptsetpref('ImShowAxesVisible','on')
iptsetpref('TruesizeWarning','off')
iptsetpref('ImshowTruesize','manual')

% Enter required inputs
alfname=input('Enter file name for base image: ','s');
fmt=alfname(end-2:end);
seqbfname=input('Enter base name for data image (i.e. img): ','s');
sseq=input('Enter first image number: ');
eseq=input('Enter last image number: ');

% Set a binarizing threshold
t=50;

% Input base image into alimgconv.m for image processing
[pic,lim]=alimgconv(alfname,t);

% Input processed base image into geomdef.m for region definition
[reg2,reg3]=geomdef(pic);

% Number of white pixels in each region of several different
% base images found using fulcal.m. The counts were averaged
% to best represent the number white pixels in each region of
% a full image.

alcnt2 = [2698 3355 3160 3294 3266 3010];
alcnt3 = [1496 1783 2013 1901 1819 1821 1853 1882 1387 1595];

% Input each data image into imgconv.m for image processing
k=1;
for j=sseq:eseq
    if j<10&j>=0
        zpad='0000';
    elseif j<100&j>=10
        zpad='000';
    elseif j<1000&j>=100
        zpad='00';
    elseif j<10000&j>=1000
        zpad='0';
    else
        zpad=''
    end
    fname=[seqbfname zpad num2str(j) '.' fmt];
    pic=imgconv(fname,lim,t);
```

```
% Input processed image and region definitons into liqcnt.m
% where number of white pixels in each region of are counted.
    [cnt2(k,:),cnt3(k,:)]=liqcnt(pic,reg2,reg3);
    k=k+1;
end

% Using data image white pixel count and base image white pixel
% count, the void fraction is calculated.
[VF2,VF3] = regvoidfrac(sseq,alcnt2,alcnt3,cnt2,cnt3);
```

```
function [pic,lim]=alimgconv(fname,t);
%%%%%%%%%%%%%%%%%%%%%%%%%%%%%%%%%%%%%%%%%%%%%%%%%%%%%%%%%%%%%%%%%%%
% alimgconv.m
% Edited by Rebecca Cullion
% 2005
%%%%%%%%%%%%%%%%%%%%%%%%%%%%%%%%%%%%%%%%%%%%%%%%%%%%%%%%%%%%%%%%%%%
% This m file reads in the base image and performs image
% processing steps.
%%%%%%%%%%%%%%%%%%%%%%%%%%%%%%%%%%%%%%%%%%%%%%%%%%%%%%%%%%%%%%%%%%%

fmt=fname(end-2:end);
pic=imread(fname,fmt);

% stretch image histogram
lim=stretchlim(pic);

% adjust image contrast
pic=imadjust(pic,lim,[0 1]);

% filter out any noise
for i=1:3
    pic=medfilt2(pic);
end

% convert image to black and white
pic=im2bw(pic,t/256);
```

```
%%%%%%%%%%%%%%%%%%%%%%%%%%%%%%%%%%%%%%%%%%%%%%%%%%%%%%%%%%%%%%%%%%%
% regdef.m
% Rebecca Cullion
% 2005
%%%%%%%%%%%%%%%%%%%%%%%%%%%%%%%%%%%%%%%%%%%%%%%%%%%%%%%%%%%%%%%%%%%
% This m file is used to define the regions of interest
%%%%%%%%%%%%%%%%%%%%%%%%%%%%%%%%%%%%%%%%%%%%%%%%%%%%%%%%%%%%%%%%%%%
close all
clear all

iptsetpref('ImShowAxesVisible','on')

% read image full of liquid
branchi = imread('img01000.bmp');
[a,b] = size(branchi);

% apply a mask to the image, mask generated in def_roi.m
mask = imread('mask.bmp');
branch = mask.*branchi;

% adjust image contrast
branchadj = imadjust(branch,stretchlim(branch),[0 1]);

% filter noise
branchfilt = medfilt2(branchadj);

% binarize image
branchbw = im2bw(branchfilt,0.2);
imshow(branchbw);

% remove all white pixels from btwn channel edges
branchedge = bwmorph(branchbw,'remove');

% select region of interest.  mouse clicks define a polygonal region
% in the photos.  outside of the polyogon all pixels are set to black.

figure(1)
[maska,xr,yr] = roipoly(branchbw);
imshow(branchedge);
grid on
hold
plot(xr,yr,'r-');
hold

% determine location of all white pixels
[i,j] = find((maska&branchedge)==1);
```

```
%find upper and lower walls

% find upper bifurcation point
c = 1;
for d = min(j):max(j);
        xu(c) = d;
        xl(c) = d;
        yu(c) = max(b-i(find(j==d)));
        yl(c) = min(b-i(find(j==d)));
        c = c+1;
end

figure(2)
plot(xu,yu,'b.',xl,yl,'r.')
grid

% find slope of line associated with upper bifurcation point
figure(3)
[masks,xrs,yrs] = roipoly(branchbw);
imshow(branchedge);
grid on
hold
plot(xrs,yrs,'r-')
hold

% determine location of all white pixels
[i,j] = find((masks&branchedge)==1);

%find upper and lower walls
cs = 1;
for ds = min(j):max(j);
        xus(cs) = ds;
        xls(cs) = ds;
        yus(cs) = max(b-i(find(j==ds)));
        yls(cs) = min(b-i(find(j==ds)));
        cs = cs+1;
end

figure(2)
plot(xus,yus,'b.',xls,yls,'r.')
grid
xcropl = [xls];
ycropl = [yls];
```

```
%perform a polynomial fit on x and y components
sat = 'n';
while sat == 'n';
    fit = input('Polynomial order: ');
    p01 = polyfit(xcrop1,ycrop1,fit);
    % determine if fit is good
    pop = polyval(p01,xcrop1);
    figure(3)
    plot(xus,yus,'b.',xls,yls,'r.',xcrop1,pop,'g+');
    grid on
    sat = input('Is the fit good? ','s');
end

% find slope of line by taking derivative of polynomial
m1 = polyder(p01);

close all

% find lower bifurcation point
figure(1)
[maskb2,xrb2,yrb2] = roipoly(branchbw);
imshow(branchedge);
grid on
hold
plot(xrb2,yrb2,'r-');
hold

% determine location of all white pixels
[i,j] = find((maskb2&branchedge)==1);

%find upper and lower walls
cb2 = 1;
for db2 = min(j):max(j);
        xub2(cb2) = db2;
        xlb2(cb2) = db2;
        yub2(cb2) = max(b-i(find(j==db2)));
        ylb2(cb2) = min(b-i(find(j==db2)));
        cb2 = cb2+1;
end

figure(2)
plot(xub2,yub2,'b.',xlb2,ylb2,'r.')
grid

% find slope of channel near lower bifurcation point
figure(1)
[masks2,xrs2,yrs2] = roipoly(branchbw);
imshow(branchedge);
grid on
hold
plot(xrs2,yrs2,'r-')
hold
```

```
% determine location of all white pixels
[i,j] = find((masks2&branchedge)==1);

%find upper and lower walls
cs2 = 1;
for ds2 = min(j):max(j);
        xus2(cs2) = ds2;
        xls2(cs2) = ds2;
        yus2(cs2) = max(b-i(find(j==ds2)));
        yls2(cs2) = min(b-i(find(j==ds2)));
        cs2 = cs2+1;
end

figure(2)
plot(xus2,yus2,'b.',xls2,yls2,'r.')
grid
xcrop2 = [xls2];
ycrop2 = [yls2];

%perform a polynomial fit on x and y components
sat = 'n';
while sat == 'n';
    fit = input('Polynomial order: ');
    p02 = polyfit(xcrop2,ycrop2,fit);
    % determine if fit is good
    pop2 = polyval(p02,xcrop2);
    figure(3)
    plot(xus2,yus2,'b.',xls2,yls2,'r.',xcrop2,pop2,'g+');
    grid on
    sat = input('Is the fit good? ','s');
end

% find slope of line by taking derivative of polynomial
m2 = polyder(p02);
```

```
function [reg2,reg3]=geomdef(pic)
%%%%%%%%%%%%%%%%%%%%%%%%%%%%%%%%%%%%%%%%%%%%%%%%%%%%%%%%%%%%%%%%%%%%
% geomdef.m
% Edited by Rebecca Cullion
% 2005
%%%%%%%%%%%%%%%%%%%%%%%%%%%%%%%%%%%%%%%%%%%%%%%%%%%%%%%%%%%%%%%%%%%%
% This m file assigns locations to the four points that form
% each region. Locations determined using regdef.m
%%%%%%%%%%%%%%%%%%%%%%%%%%%%%%%%%%%%%%%%%%%%%%%%%%%%%%%%%%%%%%%%%%%%

% k = 2 branches on left hand side of image
xk2al = [30 80 101 78.6 30];                yk2al = [193 183 334 361.6 193];
xk2bl = [109 159 128.6 101 109];            yk2bl = [178 178 359 334 178];
xk2cl = [195.1 245.1 237.5 207.9 195.1];    yk2cl = [176.1 179.9 338 358.4 176.
xk2dl = [274.5 324.5 257.9 237.5 274.5];    yk2dl = [185.5 198.5 367.6 338 185.

% k = 2 branches on right hand side of image
xk2ar = [358.3 408.3 371 335.7 358.3];      yk2ar = [207.3 220.7 370 384.7 207.
xk2br = [436.3 486.3 385.7 371 436.6];      yk2br = [236.6 253.7 405.3 370 236.

% k = 3 branches on left hand side of image
xk3bl = [33 83 80 50 33];                   yk3bl = [49 49 183 163 49];
xk3cl = [83 133 134 109 83];                yk3cl = [49 49 153 178 49];
xk3dl = [133 183 159 134 133];              yk3dl = [49 49 178 153 49];
xk3el = [183 225.7 222 195.1 183];          yk3el = [49 51.7 153 176.1 49];
xk3fl = [225.7 275.7 245.1 222 225.7];      yk3fl = [51.7 62.3 179.9 153 51.7];
xk3gl = [278 328.4 306 274.5 278];          yk3gl = [62.4 67.6 167 185.5 62.4];
xk3hl = [320 370 324.5 306 320];            yk3hl = [65 83 198.5 167 65];

% k = 3 branches on right hand side of image
xk3ar = [371.3 421.3 390 358.3 371.3];      yk3ar = [81.3 90.7 189 207.3 81.3];
xk3br = [414.7 464.7 408.3 390 414.7 ];     yk3br = [94.7 113.3 220.7 189 94.7]
xk3cr = [460.6 503.6 470 436.3 460.6];      yk3cr = [109.6 126.4 220 236.3 109.

% output matrix generation
reg2 = {xk2al yk2al; xk2bl yk2bl; xk2cl yk2cl; xk2dl yk2dl; xk2ar yk2ar; xk2br
reg3 = {xk3bl yk3bl; xk3cl yk3cl; xk3dl yk3dl; xk3el yk3el;...
        xk3fl yk3fl; xk3gl yk3gl; xk3hl yk3hl;...
        xk3ar yk3ar; xk3br yk3br; xk3cr yk3cr; };
```

```
function [pic]=imgconv(fname,lim,t);
%%%%%%%%%%%%%%%%%%%%%%%%%%%%%%%%%%%%%%%%%%%%%%%%%%%%%%%%%%%%%%%%%%%%
% imgconv.m
% Edited by Rebecca Cullion
% 2005
%%%%%%%%%%%%%%%%%%%%%%%%%%%%%%%%%%%%%%%%%%%%%%%%%%%%%%%%%%%%%%%%%%%%
% This m file reads in the data image and performs image
% processing steps.
%%%%%%%%%%%%%%%%%%%%%%%%%%%%%%%%%%%%%%%%%%%%%%%%%%%%%%%%%%%%%%%%%%%%

fmt=fname(end-2:end);

% apply a mask to the data image
rawpic =imread(fname,fmt);
mask = imread('mask.bmp');
pic = mask.*rawpic;

% adjust image contrast
pic=imadjust(pic,lim,[0 1]);

%filter out any noise
for i=1:3
    pic=medfilt2(pic);
end

% convert the image to black and white
pic=im2bw(pic,t/256);
```

```
function [cnt2,cnt3]=liqcnt(pic,reg2,reg3)
%%%%%%%%%%%%%%%%%%%%%%%%%%%%%%%%%%%%%%%%%%%%%%%%%%%%%%%%%%%%%%%%%%%
% liqcnt.m
% Edited by Rebecca Cullion
% 2005
%%%%%%%%%%%%%%%%%%%%%%%%%%%%%%%%%%%%%%%%%%%%%%%%%%%%%%%%%%%%%%%%%%%
% This m file counts the number of white pixels in each region.
%%%%%%%%%%%%%%%%%%%%%%%%%%%%%%%%%%%%%%%%%%%%%%%%%%%%%%%%%%%%%%%%%%%

% k = 2 level
% roipoly returns a region of interest in the picture
% as defined by the vectors, i.e. reg2{1,1}
cnt2(1)=sum(sum((roipoly(pic,reg2{1,1},reg2{1,2})&pic)));
cnt2(2)=sum(sum((roipoly(pic,reg2{2,1},reg2{2,2})&pic)));
cnt2(3)=sum(sum((roipoly(pic,reg2{3,1},reg2{3,2})&pic)));
cnt2(4)=sum(sum((roipoly(pic,reg2{4,1},reg2{4,2})&pic)));
cnt2(5)=sum(sum((roipoly(pic,reg2{5,1},reg2{5,2})&pic)));
cnt2(6)=sum(sum((roipoly(pic,reg2{6,1},reg2{6,2})&pic)));

% k = 3 level
for k=1:10
    cnt3(k)=sum(sum((roipoly(pic,reg3{k,1},reg3{k,2})&pic)));
end
```

```
function [VF2,VF3] = regvoidfrac(sseq,alcnt2,alcnt3,cnt2,cnt3);
%%%%%%%%%%%%%%%%%%%%%%%%%%%%%%%%%%%%%%%%%%%%%%%%%%%%%%%%%%%%%%%%%%%
% regvoidfrac.m
% Edited by Rebecca Cullion
% 2005
%%%%%%%%%%%%%%%%%%%%%%%%%%%%%%%%%%%%%%%%%%%%%%%%%%%%%%%%%%%%%%%%%%%
% This m file assigns uses the data image white pixel count
% and the base image white pixel count to determine void fraction.
%%%%%%%%%%%%%%%%%%%%%%%%%%%%%%%%%%%%%%%%%%%%%%%%%%%%%%%%%%%%%%%%%%%

[m,n] = size(cnt2);

k = sseq;
for j = 1:m
    imgno(j,:) = k;
    k = k+1;
end

% calculate void fraction
for i=1:n
    for j = 1:n
        VF2(:,j)=1-(cnt2(:,j)./alcnt2(1,j));
    end
    for j = 1:10;
        VF3(:,j)=1-(cnt3(:,j)./alcnt3(1,j));
    end
end

point = imgno(:,1);

% calculate the time-averaged void fraction of k = 2 branches
k2alvf = VF2(:,1);
avgk2alvf = mean(k2alvf);

k2blvf = VF2(:,2);
avgk2blvf = mean(k2blvf);

k2clvf = VF2(:,3);
avgk2clvf = mean(k2clvf);

k2dlvf = VF2(:,4);
avgk2dlvf = mean(k2dlvf);

k2arvf = VF2(:,5);
avgk2arvf = mean(k2arvf);

k2brvf = VF2(:,6);
avgk2brvf = mean(k2brvf);
```

```
% calculate the time-averaged void fraction of k = 3 branches
k3blvf = VF3(:,1);
avgk3blvf = mean(k3blvf);

k3clvf = VF3(:,2);
avgk3clvf = mean(k3clvf);

k3dlvf = VF3(:,3);
avgk3dlvf = mean(k3dlvf);

k3elvf = VF3(:,4);
avgk3elvf = mean(k3elvf);

k3flvf = VF3(:,5);
avgk3flvf = mean(k3flvf);

k3glvf = VF3(:,6);
avgk3glvf = mean(k3glvf);

k3hlvf = VF3(:,7);
avgk3hlvf = mean(k3hlvf);

k3arvf = VF3(:,8);
avgk3arvf = mean(k3arvf);

k3brvf = VF3(:,9);
avgk3brvf = mean(k3brvf);

k3crvf = VF3(:,10);
avgk3crvf = mean(k3crvf);
```

APPENDIX C. Instrumentation

Instrument	Manufacturer	Model	Specs
Laser	Coherent	Compass 415M-300 Diode-Pumped Laser	532 nm, 300 mW
Filter	unknown	unknown	570 nm long pass
Lens	Nikon	60mm f/2.8D AF Micro-Nikkor	min focal distance = 8.75 in
Camera	Vision Research	Phantom V5.0	1024 x 1024 @ 1000 fps 32X256 @60000 fps
Stage	Thor Labs	0.5 in travel translation stage	25.4 micron/grad
Water tank	Vanguard	Compact 6	2000 W. 6 gallon capacity
Controller	Omega	CNi-3244-DC	12 to 36 V, 3 W max
Power switching device	Omega	CNi-3244-DC	
Pump	Micropump	Series 180	0 to 150 g/min
Filter	Shelco		10 micron
Heater	McMaster	Silicone rubber heat blanket	
Mass flow meter	MicroMotion	CMF010	0 to 1370 g/min
Constant temp bath	Neslab	EX-311	800 W, 41.3x25.4x30.5 cm
RTD	Therm-X	D-SP-4TT-A18-6-36ST	0 to 250 deg C
Rope heater	McMaster	High temperature rope heater	100 W, 0.83 A
Fluke data logger	Fluke and Phillips	Fluke Hydra Data Logger	
Pressure transducer	Cole Parmer	EW-68074-08	0 to 25 psig
Vacuum pump	Air Cadet	Vacuum/Pressure Station	max vacuum = 20 in Hg
Stainless steel tubing	Swagelok		1/4" OD, 0.035 in ID
Teflon tubing			500 F, 168 psi @ 70 F
5 Power supplies	Texronix	DC Power Supply PS280	